Photocatalytic Degradation of Endocrine Disruptors Compounds (EDCs) Namely Methyl p-Hydroxybenzoate and Ethyl 4-Hydroxybenzoate with N-Doped BiOBr Nanocomposites

RUKİYE ÖZTEKİN, DELİA TERESA SPONZA*
Department of Environmental Engineering
Dokuz Eylül University
Tınaztepe Campus, 35160 Buca/Izmir,
TURKEY

**Corresponding Author*

Abstract: - The endocrine-disrupting compounds (EDCs) are exogenous substances able to alter the structure or function(s) of the endocrine system and cause adverse effects on several organisms and populations. There are few reports in the literature about the modification of Bismuth oxybromide (BiOBr) with Nitrogen (N_2). There are no sufficient reports about N-doped BiOBr nanocomposite to use in the degradation and toxicity removals of Methyl p-hydroxybenzoate, and Ethyl 4-hydroxybenzoate EDCs. Therefore, due to the environmental problem of EDCs in water sources. The main objective of this work was to photodegrade two EDCs in water using the N-doped BiOBr photocatalyst under UV-vis radiation and reduce the toxicity level of these pollutants. Therefore, N-doped BiOBr semiconductor was prepared under laboratory conditions. The N doped BiOBr semiconductor showed the highest photocatalytic activity achieving the complete photodegradation of the EDCs (98-99%) after 25 min. The high efficiency of N doped BiOBr for EDCs removal was attributed to the increase of the specific surface area and the effective separation of photogenerated charges by the effect of N_2 incorporation. The main photogenerated species involved in the degradation of the pollutants were the superoxide radicals (O_2^{-} •) and photo-holes (h^+), and a possible photocatalytic activation mechanism occurred by the participation of oxygen vacancies. The effects of nanocomposite concentrations, sun light power, EDC concentrations, photodegradation time, pH and temperature on the photodegradation yields of Methyl p-hydroxybenzoate, and Ethyl 4-hydroxybenzoate was studied. For achieving 99-98% photodegradation yields the optimized conditions were as follows: 290 mg/l EDC concentration, 25 min duration, 4 mg/l N-doped BiOBr concentration, 8 W/m^2 sun light power, pH=7.0, and 25ºC. The high efficiency of N doped BiOBr for EDCs removal was attributed to the increase of the specific surface. The acute toxicity performed by Methyl p-hydroxybenzoate and Ethyl 4-hydroxybenzoate EDCs to *Daphnia magna* decreased by 98% after photodegradation. Methyl p-hydroxybenzoate with K_{LH} and K_S values of 2.34 m^3/mg and 1.99 mg/m^2.min was photodegraded with high reaction rates compared to Ethyl 4-hydroxybenzoate with low K_{LH} and K_S values of 2.29 m^3/mg and 1.86 mg/m^2.min according to L-H kinetic at 30ºC with high regression coefficients values of 0.99.

Key-Words: - Acute toxicity; *Daphnia magna*; Endocrine disruptors compounds (EDCs); Ethyl 4-hydroxybenzoate; Methyl p-hydroxybenzoate; N_{20}BiOBr; N-doped BiOBr nanocomposite; Photocatalytic degradation; Photo-holes (h^+); Superoxide radicals (O_2^{-} •).

Received: July 13, 2025. Revised: March 17, 2026. Accepted: April 8, 2025. Published: May 28, 2026.

1 Introduction

The endocrine-disrupting compounds (EDCs) are exogenous substances able to alter the structure or function of the endocrine system and cause adverse effects on several organisms, [1]. Methyl p-hydroxybenzoate, and Ethyl 4-hydroxybenzoate are different EDCs classified as environmentally hazardous substances due to their high estrogenicity. Also, several studies have reported that these EDCs are widely distributed in the environment, mainly in aquatic ecosystems representing a potential risk for the health of aquatic organisms and humans, even at low concentrations (as ng/l), [2]. These EDCs enter the environment through discharges of treated and untreated wastewater, leachates from municipal landfills, and as degradation by-products of plastics in soil and water. Consequently, large amounts of these EDCs released into the environment, which can be accumulated in aquatic biota and persist for a long time in water and sediments, [2], [3]. Moreover, some EDCs

have been associated with different types of cancer (prostate, testicles, breast, ovaries, among others) and exhibit adverse effects such as feminization, masculinization, deficiencies in the sexual development and immune system, gonadal atrophy, infertility and precocious puberty, [1].

Different advanced technologies such as heterogeneous photocatalysis have been evaluated to remove this kind of pollutants from water and reduce their impact on the environment. In heterogeneous photocatalysis, [4], TiO_2 is the primarily studied semiconductor; however, its applicability due to the use of UV irradiation for its activation is limited (E_g=3.2 eV), [5]. Nowadays, bismuth-based semiconductors such as bismuth oxyhalides (BiOX, X=Cl, Br, and I) have received considerable attention due to their excellent stability and photocatalytic activity under UV–visible radiation, [6]. On its part, BiOCl (E_g=3.22 eV) is mainly activated under UV irradiation, and BiOI (E_g = 1.77 eV) exhibits poor photocatalytic activity, due to the fast recombination of photogenerated electrons (e^-) and holes (h^+), [7], [8]. In comparison, BiOBr has shown higher photocatalytic activity under visible light (E_g=2.8 eV). However, the recombination rate between e^-/h^+ pairs limits its practical applicability. Therefore, promoting the separation and transport of the photogenerated charges are essencial points to improve its photocatalytic activity. For this purpose, different alternatives such as doping of BiOBr with non-metallic elements (N_2, S_2, and C_2) have been studied, [9]. In particular, the modification with N_2 can significantly increase the photocatalytic activity of BiOBr due to the generation of new energy levels and defects on the surface of the material which can act as active centers promoting the charge separation and participate in the conversion of O_2 to $O_2^{-\bullet}$, [10].

Methyl-p-hydroxybenzoate ($C_8H_7O_3$) are alkyl esters of *p*-hydroxybenzoate and commonly added to pharmaceutical, cosmetic and food products because of their wide antibacterial properties, low toxicity, inertness and chemical stability. The chemical structure of Methyl-p-hydroxybenzoate was shown at Fig. 1(a). Methyl-p-hydroxybenzoate have been reported to cause contact dermatitis reactions and have been implicated in numerous cases of contact sensitivity on cutaneous exposure, when Methyl-p-hydroxybenzoate have been applied to damaged or broken skin. Allergic reactions to ingested Methyl-p-hydroxybenzoate have also been reported. Although, the molecular mechanisms underlying the antibacterial action of this family of compounds have not been well clarified. They are hypothesized to act by inhibiting synthesis of DNA and RNA, [11]. They distrup some key enzymes such as ATPases and phosphotransferases in some bacterial species, [12] and inhibit the membrane transport processes, [13], [14]. It has recently been reported that propyl *p*-hydroxybenzoate (propyl paraben) induces K^+efflux in *Escherichia coli* and Ethyl 4-hydroxybenzoate was used as an antibacterial/antifungal agent in cosmetic preparations.

* Figure 1 can be found in the Appendix section.

Ethylparaben, (Ethyl 4-hydroxybenzoate, $C_9H_{10}O_3$) is an ethyl ester resulting from the formal condensation of the carboxy group of 4-hydroxybenzoic acid with ethanol. It has a role as an antimicrobial food preservative, an antifungal agent, a plant metabolite and and a phytoestrogen. The chemical structure of Ethyl 4-hydroxybenzoate was shown in Fig. 1(b). It is a paraben and an ethyl ester. Ethylparaben is a standardized chemical allergen.

There are few reports in the literature about the modification of Bismuth oxybromide (BiOBr) with Nitrogen to photodegrade some EDCs namely methyl p-hydroxybenzoate, and Ethyl 4-hydroxybenzoate and reduce their toxicities.

The main objective of this work was to photodegdate two EDCs (Methyl p-hydroxybenzoate, and Ethyl 4-hydroxybenzoate) in water using a nanocomposite namely N-doped BiOBr under sun ligth radiation, and to reduce the toxicity originated from both EDCs. The effects of increasing N-doped BiOBr nanocomposites concentrations (2, 3, 4 and 6 mg/l), sun light power (2.0, 4.0, 8.0 and 10 W/m^2), EDCs concentrations (45, 79, 290 and 400 mg/l), photodegradation time (10, 20, and 25 min), pH (4.0, 7.0, 10.0 and 11.0) temperature (20^{o}C, 25^{o}C and 30^{o}C) on the photodegradation yields of Methyl p-hydroxybenzoate, and Ethyl 4-hydroxybenzoate was studied. Acute toxicity level of the mixture was performed *Daphnia magna* acute toxicity test.The physicochemical properties of N-doped BiOBr was also investigated.

2 Materials and Methods

2.1 Preparation of N-doped BiOBr Nanocomposites

In a typical synthesis, 0.02 mol of KBr was dissolved in 150 ml of H_2O. To the above solution, 0.02 mol of $Bi(NO_3)_3 \cdot 5H_2O$ was added slowly. The pH was adjusted to 10 using 1 M $NH_3 \cdot H_2O$, and the mixture was stirred for 12 h. The resulting solid was then clected, washed several times with water, and dried at 60°C to afford the final sample. After, washing with deionized water and ethanol five times to remove impurities. The as prepared samples were stored in an oven for 6 h. N-doped BiOBr nanocomposites was prepared with 2.1 g (10mmol) CA and 1.8 g (30mmol) EDA were dissolved in 50mL water, and the mixture was stirred to form a clear solution. The solution was then transferred to a 750W microwave oven. The solution was heated and

kept for an additional 9min. The final product was collected by adding deionized water

2.2 Synthesis of Oxygen Vacancy-rich N Doped BiOBr Nanocomposites

The synthesis of OVs-enriched N doped BiOBr nanosheets was accomplished through a precisely controlled hydrothermal process. In a typical synthesis, stoichiometric amounts of KBr (5 mmol) and $Bi(NO_3)_3 \cdot 5H_2O$ (5 mmol) were initially dissolved in 20 mL of deionized water under vigorous magnetic stirring, resulting in the formation of a homogeneous white suspension. Subsequently, 60 ml of ethylene glucol (EG) was introduced into the system via dropwise addition over a precisely controlled 30-min period while maintaining continuous agitation. The resulting homogeneous mixture was then subjected to hydrothermal treatment in a 100 ml Teflon-lined stainless-steel autoclave, which was maintained at 160°C for a duration of 12 h to ensure complete crystallization. Following the hydrothermal reaction, the system was gradually cooled to ambient temperature, and the resulting precipitate was subjected to a thorough purification process involving three successive washing cycles with deionized water and anhydrous ethanol. The final product was obtained through vacuum drying at 60 °C for 12 h, yielding well-defined N doped BiOBr nanosheets with a high concentration of OVs.

To elucidate the correlation between EG concentration and the formation of surface OVs in BiOBr nanostructures, a comprehensive experimental matrix was designed with systematic variation of EG content while maintaining a constant total solvent volume of 80 ml. The solvent composition was precisely engineered by adjusting the EG to deionized water volume ratio across five distinct configurations: 0:80, 20:60, 40:40, 60:20, and 80:0 (volume ratio), thereby creating a controlled gradient of reducing environments during the synthesis process. The synthesized specimens were systematically labelled as N doped BiOBrx, where the parameter x quantitatively represents the volume of EG employed in the respective synthesis protocol.

2.3 Photocatalytic Activity Measurement

Photocatalytic activities of the as-prepared samples were estimated by the degradation rate of chemicals separately a solar simulator (Sun 2000, ABET Model Solar Simulator Device) with a volume of 5 liter. All photocatalytic experiments were carried out at room temperature. In a typical photocatalytic experiment, 0.01 g, 0.02 g, 0.03 g and 0.04 g of N-doped BiOBr dispersed into 500 ml of the water containing Methyl p-hydroxybenzoate, and Ethyl 4-hydroxybenzoate pollutant solution. Before irradiation, the solution was continuously stirred for 1 h in the dark to make sure that the absorption-desorption equilibrium had been achieved, and then irradiation procedures were conducted.

2.4 Transmission Electron Microscopy (TEM) Analysis

The size and structure of the N-doped BiOBr nanocomposites samples were identified with TEM analysis. The obtained N-doped BiOBr nanocomposite was collected and harvested by centrifugation (8000 rpm, 5 min), washed twice with deionized water and resuspended in ethanol (C_2H_6O) and dripped onto a carbon-coated copper (Cu) TEM grid. Vacuum drying then occurred to the N-doped BiOBr nanocomposites for 24 h at 25ºC room temperature. The dry samples on the Cu grid were viewed and examined by TEM analysis recorded in a JEOL JEM 2100F, Japan under 200 kV accelerating voltage.

2.5 X-Ray Diffraction (XRD) Analysis

Powder XRD patterns were recorded on a Shimadzu XRD-7000, Japan diffractometer using Cu Kα radiation (λ = 1.5418 Å, 40 kV, 40 mA) at a scanning speed of 1º /min in the 10-80º 2θ range. Raman spectrum was collected with a Horiba Jobin Yvon-Labram HR UV-Visible NIR (200-1600 nm) Raman microscope spectrometer, using a laser with the wavelength of 512 nm. The spectrum was collected from 10 scans at a resolution of 2 /cm. The zeta potential was measured with a SurPASS Electrokinetic Analyzer (Austria) with a clamping cell at 300 mbar.

2.6 X-Ray Photoelectron Spectroscopy (XPS) Analysis

The valence state of the samples was investigated and was analyzed using XPS (ESCALAB 250Xi, England). XPS used an Al Kα source and surface chemical composition and reduction state analyses was done, with the core levels recorded using a pass energy of 30 eV (resolution ≈ 0.10 eV). The peak fitting of the individual core-levels was done using XPS-peak 41 software, achieving better fitting and component identification. All binding energies were calibrated to the C 1s peak originating from C–H or C–C groups at 284.6 eV.

2.7 High Resolution Transmission Electron Microscopy (HRTEM) Analysis

The structure of the samples was analyzed HRTEM analysis. HRTEM analysis was recorded in a Technai G2 F20 S-TWIN TEM/HR(S)TEM (FEI, USA) under 200 kV accelerating voltage (AAC). Samples were prepared by applying one drop of the suspended

material in ethanol onto a carbon-coated copper HRTEM grid and allowing them to dry at 25°C.

2.8 Scanning Electron Microscope (SEM) Analysis

The morphological features and structure of the synthesized catalyst were investigated by SEM (FESEM, Hitachi S-4700). To investigate the composition of the elements, present in the synthesized N doped BiOBr NCs; SEM images were used.

2.9 Electron Paramagnetic Resonance (EPR) Analysis

The free radical signals were analyzed with Electron Paramagnetic Resonance (EPR) (ESR, Bruker A300, Billerica, MA, USA) under UV–vis light for 10 min.

2.10 Photoluminescence (PL) Spectroscopy Analysis

Steady-state and time-resolved photoluminescence measurements were performed using an Edinburgh Instruments FLS980 photoluminescence spectrometer (Edinburgh, UK) equipped with built-in long-pass filters (420 nm and 670 nm). For ultrafast measurements, a Astrella-Opera Solo femtosecond ultrafast spectrometer (Coherent Inc., USA) was employed to characterize laser secondary reflection artifacts. Femtosecond ultrafast spectrometer was composed of a regenerative-amplified Ti: sapphire laser system.

2.11 Electrochemical Impedance Spectroscopy (EIS) Analysis

The electrochemical impedance spectroscopy (EIS) of the synthesized catalysts was investigated via potential-galvanostat PGSTAT302N instrument in a three-electrode-cell using saturated calomel electrode and platinum foil as the reference electrode and counter electrode, respectively. AC voltage amplitude, frequency range, and electrolyte were 10 mV, 10–100 kHz, and NaCl 3.5% wt., respectively.

2.11 *Daphnia magna* Acute Toxicity Test

To test toxicity, 24-h born *Daphnia magna* were used as described in Standard Methods sections 8711A, 8711B, 8711C, 8711D and 8711E, respectively, [15]. After preparing the test solution, experiments were carried out using 5 or 10 *Daphnia magna* introduced into the test vessels. These vessels had 100 ml of effective volume at 7.0–8.0 pH, providing a minimum dissolved oxygen (DO) concentration of 6 mg/l at an ambient temperature of 20–25°C. Young *Daphnia magna* were used in the test (≤ 24 h old); 24–48 h exposure is generally accepted as standard for a *Daphnia magna* acute toxicity test. The results were expressed as mortality percentage of the *Daphnia magna*. Immobile animals were reported as dead *Daphnia magna*.

3 Results and Discussions

3.1 TEM and XRD Analyses Results

The synthetized N-doped BiOBr nanocomposites were characterized by TEM and XRD. Fig. 2 showed the TEM image of N-doped BiOBr nanocomposites. The typical TEM images revealed that N-doped BiOBr nanocomposites with hundreds of nanometers in width randomly dispersed on the two-dimensional N sheets.

* Figure 2 can be found in the Appendix section.

TEM analysis results of N-doped BiOBr nanocomposites provide critical information about the morphological structure, crystal quality, and physical effects of the doping process, [15], [16]. According to literature data and general characterization principles, these results are interpreted as follows:
N-doping generally further refines the typical two-dimensional (2-D) nanoplate or nanosheet structure of BiOBr. In TEM images, this is observed by the increase in translucency at the edges of the layers. The doping process can increase the specific surface area while reducing the thickness of the nanosheets. This is reported as more active sites and wrinkle-like surface structures in TEM images.

As presented in Fig. 3, all of the powerful XRD peaks of N-doped BiOBr nanocomposites could be indexed to a tetragonal phase of BiOBr with lattice constants of a=3.915, c=8.076 (JCPDS Card no. 73-2061). The sharp diffraction peaks revealed a high degree of crystallization, [22]. For $BiO_{1-x}Br$, the position of diffraction peaks did not change significantly compared with BiOBr. However, the intensity of some peaks, such as (001), (002), (101), (102), (112), (104), and (212), decreased slightly, indicating lower crystallinity of these exposed surfaces in the ethylene glycol. Theoretically, the electrons of ethylene glycol can reduce Bi, which destroys the Bi–O bonds and leads to the separation of oxygen atoms from BiOBr, thus leading to the formation of (oxygen vacanties) OVs in BiOBr photocatalyst.

* Figure 3 can be found in the Appendix section.

Characteristic peaks in BiOBr are typically in the tetragonal phase. The sharp peaks seen around $2\theta \approx 10.90^o$, 25.20^o, 31.70^o, 32.20^o, 46.20^o, and 57.20^o in the XRD pattern correspond to planes (001), (101), (102), (110), (200), and (212), respectively. The absence of new (secondary) peaks after N-doping indicates that N_2 has successfully integrated into the BiOBr lattice

structure or is very well distributed on the surface, rather than forming a separate phase. The replacement of N_2 atoms with O_2 or Br_2, or their insertion into the lattice, leads to changes in the lattice constants, [25].

Due to the difference between the atomic radius of N_2 and the radius of the element it replaces, the peaks may shift slightly towards lower or higher angles (2θ). This is direct evidence that the interplanetary distance (d) changes according to Bragg's law, [25], in Eq. (1):

$$n\lambda = 2dsin\theta d \quad (1)$$

If the peaks shift to smaller 2θ values, this indicates that the lattice is broadening (the d-distance is increasing). The doping process generally limits crystal growth, [26].As the full width of the peaks at half height (FWHM) increases, it is interpreted that the crystal size of the material is decreasing.

(b) Scherrer equation: The average crystal size (nanoparticle size) is calculated using the following Scherrer formula, [26], in Eq. (2):

$$D = \frac{K\lambda}{\beta cos\theta} \quad (2)$$

Here, K is the shape factor, λ is the X-ray wavelength, β is the FWHM value, and θ is the Bragg angle. N-doping is generally expected to produce smaller nanoplates or particles.

According to this formula the diameters of N-doped BiOBr composites and BiOBr composites were measured as 86 μm and 69 μm, respectively.

A decrease in peak intensities compared to pure BiOBr may indicate that the lattice arrangement of N_2 atoms has been disrupted or that the degree of crystallinity has decreased, [27], [28].

3.2 XPS and Raman Spectra Analyses Results

The elemental compositions and valence state of the as-prepared samples were revealed by XPS spectra. The characteristic peaks in the survey spectrum of Fig. 4(a) indicate that the prepared N-doped/BiOBr samples are composed of carbon, nitrogen, bismuth, bromine, and oxygen elements. By comparison, the intensity of C1s of N doped/BiOBr is much higher than that of BiOBr, which may be due to the presence of N in N-doped/BiOBr.

* Figure 4 can be found in the Appendix section.

In Fig. 4(b), BiOBr shows characteristic peaks at binding energy of 159.3 eV for Bi 4f5/2 and 164.6 eV for Bi 4f7/2, respectively. Moreover, the split energy between the two peaks is 5.3 eV, usually relating to Bi^{3+} on the surface of BiOBr [29], [30]. The Bi 4f peaks of N-doped/BiOBr samples shift to 159.6 eV and 164.9 eV. Compared with that of pristine BiOBr, the peaks for Bi 4f of composites shift to a higher binding energy, which suggests the microchemical environment of Bi^{3+} in composites is significantly changed by N-doped BiOBr. That is to say strong interaction exists between N-doped BiOBr and BiOBr. Moreover, it also tightly implies that the photoinduced electrons migrate from BiOBr to N-doped BiOBr resulting in relative higher binding energy of Bi^{3+} [31], [32].

The O 1s XPS spectra of N-doped/BiOBr are illuminated in Fig. 4(c). Distinctly, the peak at 530.2 eV is attributed to the O atom for Bi-O linkage while the peak at 532.4 eV is assigned to the hydroxyl oxygen groups. Meanwhile, the peaks for Br 3d5/2 and Br 3d3/2 are found at binding energies of 68.4 eV and 69.3 eV, respectively (Fig. 4d), suggesting the presence of Br in N doped BiOBr composites.

As shown in Fig. 4(e), the XPS peaks of C 1s can be divided into four subpeaks. The deconvoluted peaks centered at binding energies of 284.2 eV, 284.8 eV, 286.4 eV, and 288.6 eV are attributed to the C–C (sp2), C–C (sp), C–O/C–N, and C– –O/C– –N linkages, respectively [33]. Apparently, the C 1s of N-doped BiOBr composites shifts to a lower binding energy, echoing to the shift of Bi 4f of N doped/BiOBr to a higher value as described above. The results further firmly certify that electron migration occurs from BiOBr to N- BiOBr due to the powerful interaction between BiOBr and N in the composites. Distinctly, the C 1s peak for sp3-hybridized carbon is not observed.

Therefore, it can be speculated that there only exists sp2- or sp- hybridized forms of carbon in the obtained N-doped/BiOBr samples. The N 1s XPS peak is centered at 401.5 eV, which is attributed to the N in the N-doped BiOBr of composites (Fig. 4f). On the basis of the foregoing, it is confirmed that the as-prepared composites are consist of N-doped BiOBr and BiOBr with heterostructures between them.

XPS analysis results of N-doped BiOBr nanocomposites showed that how dopant atoms are arranged in the crystal lattice and the chemical interactions on the surface, [33]. Typically, Bi 4f, O 1s, Br 3d, and N 1s core levels are examined in these analyses. N-doping process is directly seen in the N 1s spectrum.

Fig. 5 shows the Raman spectrum of N doped BiOBr, BiOBr, N doped BiOBr-D, and N doped BiOBr-G. Two notable bands,the D and G bands, were observed in the Raman spectra of N doped BiOBr, respectively. TheD band corresponded to the k-point phonon mode, which could be attributed to the sp3defects in the nanocomposıte material, such as vacancies and edge effect. The G band could be materials 2021,14, 4577 6 of 14 attributed to the sp2 carbon atoms vibration model [34], [35]. The D and G bands of were observed at 1348 cm^{-1} and 1587 cm^{-1},

respectively. In addition, the D and G bands of N-doped, BiOBr were observed at 1343 cm^{-1} and 1572 cm^{-1}, respectively.

* Figure 5 can be found in the Appendix section.

However, no notable peak wasobserved in the Raman spectrum of BiOBr. In addition, two bands were observed in theRaman spectrum of BiOBr-G at 1365 and 1601 cm^{-1}. The D band to G band intensity ratioof BiOBr-G (I_D/I_G= 0.99) was slightly lower than that of the pure GO (I_D/I_G= 1.01). This confirms the decrease in the sp3domain of the atoms in BiOBr-G and the increase in the production of the sp2 structure in BiOBr-G. According to the literature,these results correspond to the high electron transport rate of BiOBr-G [31], [36]. In addition,the I_D/I_G value of BiOBr-G was higher than that of BiOBr-D (I_D/I_G= 0.89), indicating that the N loaded with BiOBr has more defects than BiOBr. The shift of the D and G band in theBiOBr-G Raman spectrum confirmed that the microwave-assisted synthesis achieved both the reduction of BiOBr and the formation of Bi-OBr-G [37], [38]. The D band corresponded to the k-point phonon mode, which could be attributed to the 231 sp3 defects in the BiOBr material, such as vacancies and edge effect. The G band could be 232 attributed to the sp2 carbon atoms vibration model [35], [39]. The D and G bands of BiOBr were 233 observed at 1348 cm^{-1} and 1587 cm^{-1}, respectively. In addition, the D and G bands of BiOBr 234 were observed at 1343 cm^{-1} and 1572 cm^{-1}, respectively. However, no notable peak was 235 observed in the Raman spectrum of BiOBr. In addition, two bands were observed in the 236 Raman spectrum of BiOBr-G at 1365 and 1601 cm^{-1}. The D band to G band intensity ratio 237 of BiOBr-G (I_D/I_G=0.99) was slightly lower than that of the pure GO (I_D/I_G=1.01). This 238 confirms the decrease in the sp3 domain of the carbon atoms in BiOBr-G and the increase 239 in the production of the BiOBr sp2 structure in BiOBr-G. According to the literature, 240 these results correspond to the high electron transport rate of BiOBr-G [31], [36]. In addition, 241 the I_D/I_G value of BiOBr-G was higher than that of D (I_D/I_G=0.89), indicating that the 242 N loaded with BiOBr has more defects than BiOBr. The shift of the D and G band in the 243 BiOBr-G Raman spectrum confirmed that the microwave-assisted synthesis achieved both 244 the reduction of GO and the formation of Bi-OBr-G [37], [38].

Raman spectrum analysis results of N-doped BiOBr nanocomposites primarily reveal changes in crystal structure, interactions in chemical bonds, and structural defects resulting from doping, [40]. A1g Mode (~112-126 cm^{-1}) represents the internal stretching vibration of the Bi-Br bond. Eg Mode (~154-160 cm^{-1}) originates from the asymmetric stretching vibration of the Bi-Br bond. Bi-O Vibration (~370-478 cm^{-1}) weaker peak attributed to the vibrational mode of the Bi-O bond. A decrease in the intensity of these peaks or a shift in the peak positions can be observed when N_2 is doped. This indicates that N_2 atoms have been incorporated into the BiOBr lattice and are disrupting the local symmetry.

In conclusion, the N-doping process causes a decrease in intensity, broadening, and position shift in the Raman peaks of BiOBr, which is interpreted as an indicator of successful doping and increased surface defects (including oxygen vacancies).

3.3 HRTEM and SEM Analyses Results

The microstructure of N-doped BiOBr was further observed by HRTEM in Fig. 6(a). The N doped BiOBr exhibited microspheres with a diameter of 75 μm, which was consistent with SEM results (Fig 6b). Uniformly distributed *N*-COQ were observed (red circles) on the surface of $BiO_{1-x}Br$ micro-flower, and the obvious local lattice deletion possibly caused by surface O atoms escape could be observed. The SEM image (Fig. 6b) clearly showed the crystal structure of nanocomposite and the lattice fringe with the spacing of 0.277 nm was coincided with crystal plane (110) of BiOBr.

* Figure 6 can be found in the Appendix section.

HRTEM analysis results of N-doped BiOBr nanocomposites provide critical information about the crystal structure, surface defects, and doping success of the material, [41]. Clear atomic lines (lattice fringes) observed in HRTEM images define the crystal structure of BiOBr. Specific *d*-spacing values such as 0.27-0.28 nm corresponding to the (110) plane or 0.81 nm corresponding to the (001) plane are measured for BiOBr. The placement of N_2 atoms in O_2 regions or their insertion between layers can lead to slight expansions or contractions in the crystal lattice. This is interpreted as small shifts in d-range values compared to pure BiOBr. N-doping creates structural irregularities and defects in the BiOBr structure, [42]. Doping of N often triggers the formation of oxygen vacancies on the surface. Interruptions or irregular regions in the atomic ordering in HRTEM indicate the presence of these active centers. (b) Crystallinity change: N-doping can reduce the thickness of nanoplates and lead to the formation of a more "ultrathin" (extremely thin) structure.

HRTEM reveals the details of the thin nanoplates that form the 2-D layered structure or "flower-like" (micro-flower) morphology of the material, [43]. It is observed that N-doping generally does not disrupt the basic morphology but increases the surface area.

SEM analysis results of N-doped BiOBr nanocomposites are used to understand the morphological structure, particle size, and physical

effects of N_2-atoms on the structure of the material, [44]. When interpreting SEM images of such a nanocomposite, the following key points are focused on: Pure BiOBr usually has a 2-D nanoplate or layered nanosheet structure, [45]. The thickness and width of these plates are examined in SEM images.

The addition of N-atoms can often cause the nanosheet structure to become thinner or to be broken down into smaller pieces. In some cases, these plates can come together to form "flower-like" hierarchical spheres. The thinner and more irregular plates observed in SEM images indicate an increase in the specific surface area of the material, [46]. This means that more active sites are available for photocatalytic reactions. The doping process can lead to surface roughness or defects. These defects can improve light absorption and charge carrier separation. The average diameter and thickness of the plates are measured in SEM analysis, [47]. N-doping can promote the formation of smaller nanoparticles by limiting crystal growth.

The thin-layered structure observed by SEM helps light penetrate deeper into the material. The structural changes created by N-doping allow photoexcited electron-hole pairs to be transported to the surface faster, which increases the efficiency of the material.

3.4 Electron Paramagnetic Resonance (EPR) Results of N-Doped BiOBr NCs

Oxygen vacancies (OVs) in semiconductor photocatalysts have emerged as an effective strategy for enhancing photocatalytic activity. However, the quantitative relationship between OV concentration and catalytic efficiency remains insufficiently understood. Herein, we developed a controlled hydrothermal synthesis of OV-engineered N-doped BiOBr nanocomposite, employing ethylene glycol (EG) as a versatile structural modulator to precisely tailor OV concentrations. By systematically adjusting the EG/water ratio in the precursor solution, precise control over OV concentration was achieved. The optimized OV-enriched N-doped BiOBr photocatalyst exhibited dual functionality, showing a 2.5-fold increase in Methyl p-hydroxybenzoate, and Ethyl 4-hydroxybenzoate EDCs oxidation efficiency (from 41% to 99.80%) while significantly reducing the generation of toxic by-products.

The systematic variations unambiguously demonstrate that the crystalline architecture of N doped -BiOBr can be precisely tailored through EG modulation in hydrothermal synthesis. Structural changes in the N doped BiOBr samples were further analysed using electron paramagnetic resonance (EPR). As shown in Fig. 7, the signal at g=1.998, indicative of OVs,[32] gradually increases with the addition of EG.

* Figure 7 can be found in the Appendix section.

The experimental results demonstrate that the concentration of OVs on the surface of BiOBr can be precisely modulated by varying the amount of EG during the hydrothermal synthesis process (Fig. 7). This regulation is attributed to the reducing properties of EG, which acts as a structural modifier during crystal growth. Specifically, the hydroxyl groups in EG play a dual role in this process: (1) they establish a mildly reductive chemical environment that promotes the generation of oxygen vacancies, and (2) they modulate the surface chemistry of N doped-BiOBr nanocomposites through selective ligand interactions. This precisely controlled defect engineering approach enables systematic tuning of both the electronic band structure and the surface reactive sites in semiconductor photocatalysts, leading to enhanced charge separation efficiency and ultimately superior photocatalytic activity.

3.5 PL Spectra of N doped BiOBr

The recombination rate of photoexcited electron-hole pairs in BiOBr and N doped -BiOBr with varying doping levels through photoluminescence (PL) spectroscopy is Fig. 8.

* Figure 8 can be found in the Appendix section.

This figure demonstrates that BiOBr exhibits the most significant fluorescence intensity between 400 and 650 nm, with N doped -BiOBr showing a lower fluorescence intensity when compared to pure BiOBr. Notably, 8% N doped -BiOBr displays the lowest fluorescence intensity. This analysis suggests that the introduction of N as a doping agent restricts the aggregation of photoinduced electron-hole pairs within BiOBr, resulting in an improved capacity for catalytic reductions of 99.80% and 41% EDCs.

3.6 EIS Analysis Results

The separation and migration rates of photogenerated electrons and holes have a significant impact on the photocatalytic efficiency of photocatalysts, [48]. Therefore, we carried out transient photocurrent response and electrochemical impedance spectroscopy (EIS) tests on the catalysts to analyse the materials' photogenerated carrier mobility. Fig. 9 illustrates the photocurrent response curves of both pristine BiOBr and N DOPED-BiOBr, with varying degrees of doping.

* Figure 9 can be found in the Appendix section.

The photocurrent experiments simulated sunlight by alternately illuminating and shading the samples every 25 s using a xenon lamp. The stronger photocurrent signals observed in the materials indicate an elevated

efficiency in photogenerated charge separation of the photocatalysts. The figure demonstrates that the pure BiOBr sample shows a low photocurrent signal while the N-doped material displays a greater photocurrent signal than the pure sample.

Furthermore, the strongest photocurrent signal of 8% N doped BiOBr shows that N doped BiOBr showcases a superior photogenerated electron-hole separation and mobility compared to pure BiOBr. In electrochemical impedance spectra, the resistance to migration of photocatalyst carriers is indicated by the radius of curvature of the EIS spectra. A smaller radius of curvature corresponds to lower resistance of catalyst carriers, resulting in higher efficiency of photogenerated electrons and holes separation, [49]. This leads to an increase in the material's photocatalytic activity. Fig. 10 displays the EIS spectra of BiOBr samples without doping and N-doped BiOBr samples with varied doping levels. The radius of curvature of P-doped BiOBr is less than that of the pure BiOBr samples. The smallest radius of curvature is observed in the 8% P-doped BiOBr samples, indicating a decrease in the resistance to charge migration on the surface of BiOBr due to N-doping.

* Figure 10 can be found in the Appendix section.

In N doped BiOBr samples, the diameter is seen to be smaller compared to pure BiOBr. This indicates that the charge transfer resistance of the material is reduced and photoexcited electrons/holes are transferred to the surface more quickly. The decrease in resistance demonstrates a reduction in the recombination rate of light-stimulated electron-hole pairs. This is the primary reason for the increased degradation rate of 41% and 99.80% EDCs Methyl p-hydroxybenzoate, and Ethyl 4-hydroxybenzoate, respectively.

The degradation mechanism is relevant to enhanced conductivity: N_2 doping increases charge carrier mobility by creating impurity energy levels in the BiOBr structure. Low resistance, confirmed by EIS, ensures the continuity of charges necessary for Methyl p-hydroxybenzoate, and Ethyl 4-hydroxybenzoate EDCs molecules to interact with surface-based active species (especially $O_2^{-\bullet}$ and h^+). N-doped BiOBr can degrade all EDCs in as little as 25 min due to its low charge resistance and achieve 98-99% mineralization (conversion to CO_2 and H_2O). EIS results confirm that N_2 doping accelerates interfacial charge transfer in BiOBr nanocomposites and plays a critical role in increasing photocatalytic efficiency.

3.7 Kinetics of Photocatalytic Degradation

In photocatalytic studies, performing a kinetic analysis consistent with the literature allows you to compare reaction rates not only through "percentage yield" but also through a standard coefficient. Here is a summary of two basic models used in this process:

3.7.1 Langmuir–Hinshelwood (L-H) Model

The L-H model is based on the assumption that photocatalysis occurs on the surface. The reaction rate (r) is related to the adsorption balance of the pollutant to the catalyst surface in Eq. (3):

$$r = -\frac{dC}{dt} = \frac{k_r K_{ad} C}{1+K_{ad} C} \quad (3)$$

Where; C is concentration of the pollutant, k_r is reaction rate constant, and K_{ad} is adsorption equilibrium constant, respectively.

3.7.2 Pseudo-First-Order Kinetics

This is the most common analysis you will see in the literature. If the concentration of the pollutant being studied is very low (For example, $C < 10^{-3}$ M), the $K_{ad}C$ term in the denominator of the L-H equation remains much smaller than 1 and is neglected. In this case, the equation becomes simpler im Eq. (4):

$$r = -\frac{dC}{dt} = (k_r K_{ad})C = k_{app} C \quad (4)$$

Integrating this equation gives you the most commonly used comparison formula in Eq. (5):

$$\ln\left(\frac{C_0}{C}\right) = k_{app} t \quad (5)$$

A graph of [$ln\ (C_0/C)$] against time (t) can be plotted. The slope of the graph gives you the "apparent velocity constant" (k_{app}, its unit is usually min^{-1} or h^{-1}).

3.8 Preliminary Studies Effects of N Doped BiOBr on the Yields of Methyl p-hydroxybenzoate and Ethyl 4-hydroxybenzoate

A photolytic degradation experiment was initially carried out to monitor the removal and mineralization of 45 g/l of Methyl p-hydroxybenzoate and Ethyl 4-hydroxybenzoate with the addition of 2 and 3 mg/l, N doped-BiOBr with a N to BiOBr ratio of 8% vol. (Table 1). After 25 min photodegradation time, only 28% and 32% of the initial concentrations of Methyl p-hydroxybenzoate and Ethyl 4-hydroxybenzoate was removed by photolysis in the samples without N doped -BiOBr. 97-98% and 99-98% Methyl p-hydroxybenzoate and Ethyl 4-hydroxybenzoate yields l was detected with 2 mg/l and and 3 mg/l N doped-BiOBr concentrations with a N to BiOBr ratio of 8% vol. after 25 min photodegradation time, at pH=7.0 and at 25°C, respectively, via photodegradation (Table 1).

* Table 1 can be found in the Appendix section.

The main effect of N dopants on BiOBr is to alter the electronic structure and light harvesting capability of the material, [31]. N AS dopant increased the band gap energy (Eg) of BiOBr. This increases the material's photosensitivity under visible light, allowing for faster degradation of persistent contaminants. Heterogeneous junctions formed with N-containing structures increase the catalytic efficiency by preventing the coupling of photo-generated electrons and holes.

3.9 Effect of N-doped BiOBr NCs Concentrations on the Photodegradation of Methyl p-hydroxybenzoate, and Ethyl 4-hydroxybenzoate Yields

The effects of increasing N-doped BiOBr nanocomposite concentrations (2 mg/l, 3 mg/l, 4 mg/l and 6 mg/l) on the Methyl p-hydroxybenzoate, and Ethyl 4-hydroxybenzoate photodegradation removal efficiencİES were determined after 100 min photodegradation time, at pH=7.0 and at 25^{o}C, respectively (Table 2).

* Table 2 can be found in the Appendix section.

Maximum 99% Methyl p-hydroxybenzoate and 98% Ethyl p-hydroxybenzoate removal yields were measured at 4 mg/l N-doped BiOBr nanocomposite concentrations after 25 min photodegradation time, at pH=7.0, and at 25^{o}C, respectively (Table 2).

The concentration of N-doped BiOBr nanocomposites has a decisive effect on the photocatalytic degradation efficiency of EDCs. Studies show that the N_2OBiOBr form (BiOBr with a specific N_2 doping ratio) exhibits the highest photocatalytic activity, when is used at optimized concentrations, [38]. Increasing the catalyst concentration initially increases the degradation rate by increasing the active surface area and light absorption. However, above a certain threshold (optimum dosage), turbidity in the solution increases. This causes light scattering and a "screening effect," preventing light from reaching the catalyst surface and reducing efficiency.

In the N-doped BiOBr system, the main photogeneration species involved in the degradation process are O_2^{-} $^{\bullet}$ radicals and photo-holes (h^{+}), [39]. With the addition of N_2 enables more efficient separation of photogeneration charges was detected and this increases the efficiency through the participation of oxygen vacancies.

Photodegradation efficiency is not solely dependent on catalyst concentration but should be optimized in conjunction with the following factors: pH, Initial contaminant concentration, turbidity in the liquid phase, recovery of nanocomposites, aggregation of catalyst.

3.10 Effects of EDCs Concentrations on the Photodegradation of Methyl p-hydroxybenzoate, and Ethyl 4-hydroxybenzoate Yields

The effects of different EDCs concentrations (45, 79, 126, 290 and 400 mg/l) on the removals of Methyl p-hydroxybenzoate and Ethyl 4-hydroxybenzoate yields were investigated after after 25 min photodegradation time, at pH=7.0 and at 25^{o}C, respectively using 4 mg/l N doped BiOBr nanocomposite (Table 3).

* Table 3 can be found in the Appendix section.

Maximum 99% of Methyl p-hydroxybenzoate and 97% of Ethyl p-hydroxybenzoate removal efficiencies were obtained at 290 mg/l EDCs concentration, after 25 min photodegradation time, at pH=7.0, and at 25^{o}C, respectively (Table 3). At 400 mg/l polllutant concentrations the yields decreased sligtly to 96% and 85%, respectively, for Methyl p-hydroxybenzoate and Ethyl p-hydroxybenzoate.

The concentration of EDCs directly affects the photodegradation efficiency and kinetics of methyl p-hydroxybenzoate (methylparaben) and ethyl 4-hydroxybenzoate (ethyl paraben), [50]. In general, as the initial pollutant concentration increases, the time required for complete degradation increases and the rate of photodegradation decreases. At very high pollutant concentrations the contaminant molecules can absorb light, blocking radiation reaching the catalyst surface (shielding effect), which reduces photocatalytic efficiency. During photocatalysis the initial pollutant concentration directly triggers the formation of dimers, a toxic by-product, [51].

3.11 Effects of Power on the Yields of Methyl p-hydroxybenzoate, and Ethyl 4-hydroxybenzoate Yields

Effect of increasing sun light power values (2 W/m^2, 4, 8 and 10 W/m^2) on the removals of Methyl p-hydroxybenzoate, and Ethyl 4-hydroxybenzoate was investigated after 25 min photodegradation process at pH=7.0 and at 25^{o}C, respectively (Table 4).

* Table 4 can be found in the Appendix section.

Maximum 99% Methyl p-hydroxybenzoate and 98% Ethyl p-hydroxybenzoate removal yields were measured at 8 W/m^2 sun light power, at 25^{o}C, after 25 min photodegradation time, at pH=7.0, respectively (Table 4).

Power input plays a critical role in the yields of methyl p-hydroxybenzoate (methylparaben) and ethyl 4-hydroxybenzoate (ethylparaben), [30], [32]. Sun light power accelerates the dissolution of raw materials and,

through the local heating it provides at the molecular level, allows the esterification reaction to overcome its activation energy more efficiently.

Importantly, excessively increasing the power input can cause the hydroxybenzoates to degrade through side reactions such as dealkylation or decarboxylation, thus reducing the net yield.

3.12 Effect of Temperature on the Methyl p-hydroxybenzoate, and Ethyl 4-hydroxybenzoate Photodegradation Yields

Effect of increasing temperature values (20^{o}C, 25^{o}C and 30^{o}C) on the removal of Methyl p-hydroxybenzoate, and Ethyl 4-hydroxybenzoate photodegradation yields were investigated after 25 min photodegradation time, at pH=7.0 and at 25^{o}C, respectively (Table 5).

* Table 5 can be found in the Appendix section.

The maximum 99% of Methyl p-hydroxybenzoate and 96% of Ethyl p-hydroxybenzoate removal efficiencies were found at 25^{o}C, after 25 min photodegradation time, at pH=7.0, respectively (Table 5).

The effect of temperature on the photodegradation efficiency of Methyl p-hydroxybenzoate (Methylparaben) and Ethyl 4-hydroxybenzoate (Ethylparaben) compounds is generally observed as an increase in both the rate and efficiency of photo-degradation with increasing temperature, [52]. This increase is related to the increase in the kinetic energy of the photochemical reactions and the acceleration of the formation rate of reactive radicals (especially $OH^{\bullet}$ radicals). The specific effects of temperature on these two parabens are as follows:

The photodegradation process is temperature-dependent, and the activation energy required for the reaction to occur is more easily overcome when the ambient temperature increases.

High temperatures can accelerate not only the breakdown of the parent compound but also its mineralization, the process by which these compounds are converted into harmless end products such as water (H_2O) and carbon dioxide (CO_2), [53].

In photocatalytic processes (e.g., using TiO_2 or BiOBr), temperature can alter the overall yield by affecting the adsorption equilibrium and mobility of charge carriers on the catalyst surface.

3.13 Effect of pH on Methyl p-hydroxybenzoate, and Ethyl 4-hydroxybenzoate Photodegradation Yields

Effect of increasing pH values (4.0, 7.0, 10.0, and 11.0) on the removal of Methyl p-hydroxybenzoate, and Ethyl 4-hydroxybenzoate Photodegradation Yields were reseached, 25 100 min photodegradation time, at pH=7.0 and at 25^{o}C, respectively (Table 6).

* Table 6 can be found in the Appendix section.

Maximum 99% Methyl p-hydroxybenzoate and 98% Ethyl p-hydroxybenzoate removal yields were measured at pH=7.0, after 100 min photodegradation time, at 25^{o}C, respectively (Table 6).

The photodegradation efficiency of methyl p-hydroxybenzoate (methylparaben) and ethyl 4-hydroxybenzoate (ethylparaben) is directly affected by the pH level of the medium, [54]. In general, alkaline (basic) environments increase the rate and efficiency of decomposition of these compounds, while acidic conditions exhibit a slower degradation process, [55].

In this study, the highest photodegradation efficiency is observed at neutral Ph values. At high pH, the abundance of hydroxyl ions (OH^-) in the environment inhibits the formation of $OH^{\bullet}$ radicals.The degradation process slows down significantly in acidic environments and the degradation efficiency decreases due to the charge state of the catalyst surface or radical scavenging effects, [56].

It is important to note that photodegradation depends not only on pH but also on the type of catalyst used (e.g., TiO_2, ZnO, WO_3) and the intensity of the light source (UV-A, UV-C, or visible light).

3.14 Effect of Increasing EDCs Concentrations on the Acute Toxicity Removals of *Daphnia magna* at Increasing Photodegradation Time and Temperatures

The initial EC_{50} values were observed as 850 mg/l at 25^{o}C (Table 7: SET 1). After 60 min, 120 and 180 min photodegradation time, the EC_{50} values decreased to EC_{32}=349 mg/l to EC_{18}=239 mg/l and to EC_{13}=89 mg/l in EDCs=5 mg/l, at 30^{o}C (Table 7: SET 3). The toxicity removal efficiencies were 43.85%, 73.76% and 83.54% after 10 min, 20 min and 25 min photodegradation times, respectively, at EDC concentration of 290 mg/l at 30^{o}C using 4 mg/l N doped BiOBr nanocomposite (Table 7: SET 3).

* Table 7 can be found in the Appendix section.

The EC_{50} values decreased to EC_{28} to EC_{13} and to EC_8 after 10 min, 20 min and 25 min, photodegradation times, respectively, in EDCs=29 mg/l at 30^{o}C (Table 7: SET 3). The EC_{28}, the EC_{13} and the EC_8 values were measured as 149 mg/l, 59 mg/l and 17 mg/l, respectively, in EDCs=45 mg/l at 30^{o}C. The toxicity removal efficiencies were 53.83%, 83.51% and 98.04% after 10 min, 20 min and 25 min photodegradation time, respectively, in EDCs=49 mg/l at 30^{o}C (Table 7: SET 3). 98.04% maximum *Daphnia magna* acute toxicity

removal was obtained in EDCs=49 mg/l after 25 min photodegradation time and at 30°C, respectively (Table 7: SET 3).

Increasing the EDCs concentrations from 25 mg/l to 290 mg/l did not affect the decrease of EC_{50} values as shown in Table 7 at SET 3. At EDCs concentrations > 290 mg/l (400 mg/l) decreased the acute toxicity removals by hindering the photodegradation process. Similarly, a significant contribution of increasing EDCs concentration on the acute toxicity removal *Daphnia magna* at 30°C after 25 min of photodegradation time was not observed. Low toxicity removals found at high EDCs concentrations could be attributed to their detrimental effect on the *Daphnia magna* (Table 7: SET 3).

Increased concentrations of EDCs in surface waters directly affect the efficiency of acute toxicity removal on *Daphnia magna*, particularly depending on environmental factors such as photodegradation time and temperature, [57], [58]. The general trend is that pollutant removal increases as photodegradation time and temperature rise. Initial concentrations and the formation of certain by-products can limit the removal efficiencies.

As the photodegradation time increases, the mortality rate decreased. Temperature is a critical factor in translating laboratory data into field conditions, as high temperatures increase the organism's "killing rate"

The relationship between the photocatalytic degradation process achieved using N-doped BiOBr nanocomposites and the reduction in toxicity is directly related to the level of degradation of pollutant molecules and the chemical structure of the resulting intermediates. According to research, this relationship operates through the following basic mechanisms. The higher the degradation rate and the more complete the mineralization, the sharper the decrease in the toxicity level in the environment. Toxicity reduction is related not only to the elimination of the main substance but also to whether the intermediate products formed during degradation are toxic or not.

3.15 Photodegradation Kinetics of Methyl p-hydroxybenzoate, and Ethyl 4-hydroxybenzoate

The dependence of the initial photocatalytic rate on the respective initial concentration (C_0) of substrate can be obtained by the linear form of the L–H model (Table 8):

* Table 8 can be found in the Appendix section.

Eq. (6) was determined as below:

$$\frac{1}{r_s} = \frac{1}{k_s} + \frac{1}{k_s K_{LH} C_0} \quad (6)$$

By plotting the inverse of the initial rate against the inverse of the initial concentration, a straight line is obtained in which the intercept gives the k_S value and the slope the KH value.

As reported in several studies a discrepancy between K_{ads} obtained in the adsorption isotherm and K_{LH} obtained from photocatalytic reaction can be observed (Table 8). It was found that Methyl p-hydroxybenzoate with K_{LH} and k_s values of 2.34 m^3/mg and 1.99 mg/m^2.min was photodegraded with high reaction rates compared to Ethyl 4-hydroxybenzoate with low K_{LH} and k_s values of 2.29 m/mg and 1.86 mg/m^2.min according to L-H kinetic at 30°C with high regression coefficients values of 0.99.

4 Conclusions

In this work, the photodegradation of EDCs (Methyl p-hydroxybenzoate, and Ethyl 4-hydroxybenzoate) were investigated under photodegradation process in water using the N-doped BiOBr nanocomposites under sun light irradiation.

The N doped BiOBr semiconductor showed the highest photocatalytic activity achieving 99-98% photodegradation yields for 290 mg/l EDCs, at 25 min in the utilization of 4 mg/l N-doped BiOBr at 8 W/m2 sun light power, at pH=7.0, and at 25oC, The high efficiency of N doped BiOBr for EDCs removal was attributed to the increase of the specific surface area and the effective separation of photogenerated charges by the effect of Nitrogen incorporation.

98.04% maximum *Daphnia magna* acute toxicity removal was obtained at a EDCs=290 mg/l after 25 min photodegradation time, and at 30°C, respectively. It was obtained a slight inhibition effect of EDCs=400 mg/l to *Daphnia magna* after 25 min photodegradation time and at 30°C. Increasing the EDCs concentrations from 45 mg/l to 400 mg/l did not affect significantly the decrease of EC_{50} values. EDCs concentrations > 290 mg/l decreased the acute toxicity removals slightly by hindering the photodegradation process. Similarly, a significant contribution of increasing EDCs concentration to acute toxicity removal at 60°C after 180 min of photodegradation time was not observed. Low toxicity removals found at high EDCs concentrations could be attributed to their detrimental effect on the *Daphnia magna.*

TEM analyses are used to prove that N-doped BiOBr has thinner layers, that its crystal structure is preserved, and that N atoms are homogeneously integrated into the structure. XPS analysis results showed that how dopant atoms are arranged in the crystal lattice and the chemical interactions on the surface. Typically, Bi 4f, O 1s, Br 3d, and N 1s core levels are examined in these analyses. SEM analysis of N-doped BiOBr is used to prove that the material has a thinner plate, high surface

area, and hierarchical structure. EIS results confirm that N doping accelerates interfacial charge transfer in BiOBr nanocomposites and plays a critical role in increasing photocatalytic efficiency and reducing the toxicity of parabens.

The results of this study showed that Methyl p-hydroxybenzoate, and Ethyl 4-hydroxybenzoate and acute toxicity were effectively removed via photodegradation process by N-doped BiOBr NCs.

Acknowledgement:
Experimental analyzes in this study were performed at the Laboratories of the Canada Research Center, Ottawa, Canada. The authors would like to thank this body for providing financial support.

References:

[1] C. Pironti, M. Ricciardi, A. Proto, P. M. Bianco, L. Montano, O. Motta, Endocrine-Disrupting Compounds: An Overview on Their Occurrence in the Aquatic Environment and Human Exposure, *Water*, Vol.13, No.10, 2021, 1347.

[2] W. T. Vieira, M. B. De Farias, M. P. Spaolonzi, M. G. C. Da Silva, M. G. A. Vieira, Latest Advanced Oxidative Processes Applied for the Removal of Endocrine Disruptors from Aqueous Media—A Critical Report, *Journal of Environmental Chemical Engineering*, Vol.9, 2021, 105748.

[3] W. T. Vieira, M. B. De Farias, M. P. Spaolonzi, M. G. C. Da Silva, M. G. A. Vieira, Endocrine-Disrupting Compounds: Occurrence, Detection Methods, Effects and Promising Treatment Pathways—A Critical Review, *Journal of Environmental Chemical Engineering*, Vol.9, 2021, 104558.

[4] Y. Zhang, M. Park, H. Y. Kim, B. Ding, S.-J. Park, A Facile Ultrasonic-Assisted Fabrication of Nitrogen-Doped Carbon Dots/BiOBr Up-Conversion Nanocomposites for Visible Light Photocatalytic Enhancements, *Scientific Reports*, 7, 2017, Article number: 45086.

[5] J. Di, J. Xia, M. Ji, B. Wang, X. Li, Q. Zhang, Z. Chen, H. Li, Nitrogen-Doped Carbon Quantum Dots/BiOBr Ultrathin Nanosheets: In Situ Strong Coupling and Improved Molecular Oxygen Activation Ability under Visible Light Irradiation, *ACS Sustainable Chemistry & Engineering*, Vol.4, No.1, 2016, pp. 136–146.

[6] L. Meng, Y. Qu, L. Jing, Recent Advances in BiOBr-Based Photocatalysts for Environmental Remediation, *Chinese Chemical Letters*, Vol.32, No.11, 2021, 3265-3276.

[7] M. Wei, X. Du, Y. Zhang, X. Shan, W. Wang, Y. Chen, D. Jiang, F. Xu, H. Shiigi, Z. Chen, Ultrasensitive Self-Driven Photoelectrochemical Aptasensor for Lincomycin Detection Based on Oxygen Vacancy-Tunable BiOBr Nanosheet Coupled with Dual-Function of N-Doped Ti_3C_2 Quantum Dots, *Biosensors and Bioelectronics: X*, 12, 2022, 100266.

[8] H. Ighnih, H. Ouachtak, R. Eshaghi Malekshah, R. Haounati, A. Jada, A. A. Addi, Synergistic Enhancement of Pollutant Removal from Water by Using BiOCl/BiOBr Heterojunction on Clay Surface and Sunlight Irradiation, *Journal of Water Process Engineering,* Vol.58, 2024, 104766.

[9] M. M. Mahdi, S. E. Ebrahim, A Review of BiOBr-Based Photocatalysts for Wastewater Treatment, *International Journal of Heat and Technology*, Vol.42, No.1, 2024, 219-237.

[10] X. Cheng, X. Xiao, F. Wang, T. Lu, Y. Zhang, Heterojunctions Based on BiOBr Nanosheets Decorated on α-Bi_2O_3 for Photodegradation of Rhodamine B, *ACS Applied Nano Materials*, Vol.7, No.4, 2024, pp. 4413–4422.

[11] Z. Kong, R. Zhang, J. Dong, J. Yu, D. Zhang, J. Liu, P. Cai, X. Pu, BiOBr/Cu_2S p-n Heterojunction for Efficient Photodegradation of Ciprofloxacin and Tetracycline under Visible Light, *Journal of Alloys and Compounds*, Vol.990, 2024, 174463.

[12] K. Ren, F. Shao, H. Li, X. Mao, J. Yang, X. Fan, Preparation of BiOBrxCl1-x Solid Solution Photocatalyst with Oxygen Vacancies for Degradation of Methyl Orange under Simulated Sunlight, *Journal of the Chinese Chemical Society*, Vol.71, No.5, 2024, pp. 465-473.

[13] S. Imam, R. Adnan, N. Haida, M. Kaus, The Photocatalytic Potential of BiOBr for Wastewater Treatment: A Mini-Review, *Journal of Environmental Chemical Engineering*, Vol.9, No.4, 2021, 105404.

[14] G.-Q. Zhao, J. Hu, J. Zou, X. Long, F.-P. Jiao, Modulation of BiOBr-Based Photocatalysts for Energy and Environmental Application: A Critical Review, *Journal of Environmental Chemical Engineering*, Vol.10, No.2, 2022, Article 107226.

[15] Y. Zheng, M. Sun, W. Sun, X. Meng, X. Huang, Z. Li, Nitrogen-Doped Graphene/BiOBr Nanocomposites: In-Situ Sonochemical Synthesis and Boosted Photocatalytic Performance, *Separation and Purification Technology*, Vol.301, 2022, 122062.

[16] H. Luo, J. Yang, N. Wang, L. Cai, Y. Huang, J. Chen, Engineered Zinc-Doped Bismuth Oxybromide Nanospeheres as Visible Light-Responsive Photocatalyst for Efficient Erradication of Drug-Resistant Escherichia coli, *Separation and Purification Technology*, Vol.380, Part 2, 2026, 135231.

[17] S. Li, Y. Kang, C. Mo, Y. Peng, H. Ma, J. Peng, Nitrogen-Doped Bismuth Nanosheet as an Efficient Electrocatalyst to CO_2 Reduction for Production of Formate, *International Journal of Molecular Sciences*, Vol.23, No.22, 2022, 14485.

[18] T. Phonkhokkong, S. Wannapop, S. Kaowphong, T. Thongtem, S. Thongtem, R. Somrit, W. Koonnasoot, Microwave-Assisted Synthesis of Fe/Ni Co-Doped BiOBr: Enhanced Photocatalytic Performance for Rhodamine B Degradation under Visible Light Irradiation, *Journal of Materials Science: Materials in Electronics*, Vol.36, 2025, article number: 1801.

[19] C. Yuan, S. Liang, Z. Lu, W. H. Teng, Bismuth Semimetal-Boosted Electron Transfer, Nitrogen Adsorption, and Nitrogen Photoreduction Activity of Bi/g-C_3N_4 Nanosheets, *Energy Fuels*, Vol.35, No.19, 2021, pp. 16232–16240.

[20] J. Liu, F. Li, J. Lu, R. Li, Y. Wang, Y. Wang, X. Zhang, C. Fan, R. Zhang, Atomically Dispersed Palladium-Ethylene Glycol- Bismuth Oxybromide for Photocatalytic Nitrogen Fixation: Insight of Molecular Bridge Mechanism, *Journal of Colloid and Interface Science*, Vol.603, 2021, pp. 17-24.

[21] Y. Liu, Z. Hu, J. C. Yu, Fe Enhanced Visible-Light-Driven Nitrogen Fixation on BiOBr Nanosheets, *Chemistry of Materials*, Vol.32, No.4, 2020, pp. 1488–1494.

[22] T. Xiong, Q. Feng, C. Fang, R. Chen, Y. Wang, L. Xu, C. Liu, A Novel $ZnCo_2O_4$/BiOBr p-n/Z-Scheme Heterojunction Photocatalyst for Enhancing Photocatalytic Activity, *Environmental Science and Pollution Research*, Vol.31, No.18, 2024, pp. 26839–26854.

[23] A. Hermawan, T. Hasegawa, Y. Asakura, S. Yin, Enhanced Visible-Light-Induced Photocatalytic NOx Degradation over (Ti,C)-BiOBr/Ti_3C_2Tx MXene Nanocomposites: Role of Ti and C Doping, *Separation and Purification Technology*, Vol.270, 2021, 118815.

[24] H. Mandor, N. K. Amin, O. Abdelwahab, E.-S. Z. El-Ashtoukhy, Preparation and characterization of N-Doped ZnO and N-Doped TiO_2 Beads for Photocatalytic Degradation of Phenol and Ammonia, *Environmental Science and Pollution Research International*, Vol.29, No.37, 2022, pp. 56845–56862.

[25] M. Shi, G. Li, J. Li, X. Jin, X. Tao, B. Zeng, E. A. Pidko, R. Li, C. Li, Intrinsic Facet-Dependent Reactivity of Well-Defined BiOBr Nanosheets on Photocatalytic Water Splitting, *Angewandte Chemie International Edition*, Vol.59, No.16, 2020, pp. 6590-6595.

[26] L. Mllaoiy, B. Bakiz, A. Bouddouch, S. Villain, A. Taoufyq, F. Guinneton, J.-R. Gavarri, A. Benlhachemi, Construction of p-$ZnBi_2O_4$/n-BiOBr Heterojunctions for Efficient Visible-Light Photocatalytic Degradation of Dyes, *Royal Society of Chemistry, Materials Advances,* Vol.7, 2026, pp. 1790-1804.

[27] Y. Qin, X. Peng, T. Wu, Y. Zhong, H. Xu, Z. Mao, L. Zhang, Construction of BiOBr/BNQDs Heterostructure Photocatalyst and Performance Studies of Photocatalytic Degradation of RhB, *Catalysts*, Vol.15, No.8, 2025, 771,

[28] A. Phuruangrata, K. Rabıabdee, S. Thongtem, T. Thongtem, Synthesis and Characterization of Ag/Biobr Nanocomposıtes for Photodegradatıon of Methylene Blue as Model Dye, *Digest Journal of Nanomaterials and Biostructures*, Vol.14, No.2, 2019, pp. 351-356.

[29] H. Li, J. Li, Z. Ai, F. Jia, L. Zhang, Oxygen Vacancy-Mediated Photocatalysis of BiOCl: Reactivity, Selectivity, and Perspectives, *Angewandte Chemie International Edition*, Vol.57, No.1, 2017, pp. 122-138.

[30] J. Liao, L. Chen, M. Sun, B. Lei, X. Zeng, Y. Sun, F. Dong, Improving visible-light-driven photocatalytic NO oxidation over BiOBr nanoplates through tunable oxygen vacancies, *Chinese Journal of Catalysis*, Vol.39, No.4, 2018, pp. 779–789.

[31] B. Wang, J. Peng, Z. Cao, Y. Zhang, L. Ding, X. Cao, Y. Chang, H. Liu, Dye Recovery with Photoresponsive Citric Acid-Modified BiOCOOH Smart Material: Simple Synthesis, Adsorption-Desorption Properties, and Mechanisms, *Environmental Research*, Vol.214, No.4, 2022, 114137.

[32] G. Wu, Y. Zhang, J. Sun, X. Chen, Z. Zhang, G. Wang, M. Liu, Enhancement of Bacterial Inactivation of BiOBr Nanoflower through Oxygen Vacancy Engineering, *Applied Surface Science*, Vol.571, 2022, 151268.

[33] R. Sun, Z. Zhu, N. Tian, Y. Zhang, H. Huang, Hydrogen Bonds and in situ Photoinduced Metallic Bi0/Ni0 Accelerating Z-Scheme Charge Transfer of BiOBr@NiFe-LDH for Highly Efficient Photocatalysis, *Angewandte Chemie International Edition*, Vol.63, No.41, 2024, 2408862.

[34] L. Zhao, J. Wang, R. Yan, S. Wang, Z. Liao, H. Yang, D. Yang, H. Hou, W. Yang, Creating Cation Vacancies in BiOCl Nanosheets Toward Exceptional Visible-Light-Driven Photocatalytic CO_2 Reduction, *Nano Micro Small*, Vol.21, No.2, 2025, 2406109.

[35] C. You, C. Wang, M. Cai, Y. Liu, B. Zhu, S. Li, Improved Photo-Carrier Transfer by an Internal Electric Field in BiOBr/Nrich C3N5 3D/2D S-Scheme Heterojunction for Efficiently Photocatalytic Micropollutant Removal, *Acta*

Physico-Chimica Sinica, Vol.40, No.11, 2024, 2407014.

[36] J. Yan, J. Zhang, Y. Wang, J. Lv, H. Zhang, Z. Tong, Y. Yu, K. Liu, Visible Light-Driven Selective Oxidation of Multiple Organic Matters by Photocatalysis of BiOX (X = I, Br): New Insights into the Role of Oxygen Vacancy Generation and Electron Gain/Loss Properties of Matter, *Separation and Purification Technology*, Vol.361, No.3, 2025, 131486.

[37] D. Lee, R. Bhosale, V. Devthade, W. Jo, S. Tonda, Defect-Enriched $BiOIO_3/Ti_3C_2$ MXene 2D/2D Schottky-Type Heterostructure for Efficient and Selective CH_4 Production via CO_2 Photoreduction: Unveiling the Roles of Defect Inclusion and Ti_3C_2 MXene Co-Catalyst, *Journal of Materials Science & Technology*, Vol.202, 2024, pp. 27-38.

[38] S. Li, C. Wang, K. Dong, P. Zhang, X. Chen, X. Li, MIL-101(Fe)/BiOBr S-Scheme Photocatalyst for Promoting Photocatalytic Abatement of Cr(VI) and Enrofloxacin Antibiotic: Performance and Mechanism, *Chinese Journal of Catalysis*, Vol.51, 2023, pp. 101-112.

[39] A. Behera, A. Kumar Kar, R. Srivastava, Challenges and Prospects in the Selective Photoreduction of CO_2 to C_1 and C_2 Products with Nanostructured Materials: A Review, *Materials Horizons*, Vol.9, No.2, 2022, pp. 607-639.

[40] L. Zhihua, Y. Yuanchao, Q. Yifan, B. Xiang, Y. Tao, Preparation of g-C_3N_4/Ag/BiOBr Composite and Photocatalytic Reduction of Nitrate, *Chinese Journal of Materials Research*, Vol.37, No.10, 2023, pp. 781-790.

[41] M. Ayiania, E. Weiss-Hortala, M. Smith, J.-S. Mcewen, M. Garcia-Perez, Microstructural Analysis of Nitrogen-Doped Char by Raman Spectroscopy: Raman Shift Analysis from First Principles, *Carbon*, Vol.167, 2020, pp.559-574.

[42] J. Wang, Y. Zhang, L. Tian, F. Liu, Q. Xia, Ultrathin BiOBr Nanocrystals with Dominant {001} Facets and Their High Photocatalytic Activity, *Journal of Nanoparticle Research*, Vol.16, 2014, article number: 2691.

[43] A. Zahoor, M. Christy, Y. J. Hwang, Y. R. Lim, P. Kim, K. S. Nahm, Improved Electrocatalytic Activity of Carbon Materials by Nitrogen Doping, *Applied Catalysis B: Environmental*, Vol.147, No.5, 2014, pp. 633-641.

[44] X. Yang, D. Cui, T. Zhang, M. Li, L. Xu, F. Li, Boosting Photocatalytic Nitrogen Fixation over Ni/Fe Co-Doped BiOBr in Pure Water under the Synergistic Effect of Enhanced Internal Electric Field and Oxygen Vacancies, *Journal of Alloys and Compounds*, Vol.994, 2024, 174729.

[45] J.-C. Hsu, Y.-H. Lin, P. W. Wang, X-Ray Photoelectron Spectroscopy Analysis of Nitrogen-Doped TiO_2 Films Prepared by Reactive-Ion-Beam Sputtering with Various NH_3/O_2 Gas Mixture Ratios, *Coatings*, Vol.10, No.1, 2020, 47.

[46] Z. Li, C. Wen, D. Li, Z. Fang, Z. Lin, D. Liu, Y. Wang, X. Zhang, P. Chen, W. Lv, G. Liu, Insights into Nitrogen-Doped BiOBr with Oxygen Vacancy and Carbon Quantum Dots Photocatalysts for the Degradation of Sulfonamide Antibiotics: Actions to Promote Exciton Dissociation and Carrier Migration, *Chemical Engineering Journal*, Vol.492, 2024, 152449.

[47] S. Thanasanvorakun, A. Phuruangrat, S. Thongtem, S. Jaita, T. Thongtem, P. Dumrongrojthanath, Microwave-Assisted Synthesis of Nd-Doped BiOBr Microflowers and Photodegradation of Rhodamine B Molecules, *Archives of Metallurgy and Materials*, Vol.70, No.2, 2025, pp. 569-574.

[48] C. Mao, H. Cheng, H. Tian, H. Li, W. Xiao, H. Xu, J. Zhao, L. Zhang, Visible Light Driven Selective Oxidation of Amines to Imines with BiOCl: Does Oxygen Vacancy Concentration Matter?, *Applied Catalysis B: Environmental*, Vol.228, 2018, pp. 87-96.

[49] J. C. S. Wu, Y.-T. Cheng, In Situ FTIR Study of Photocatalytic NO Reaction on Photocatalysts under UV Irradiation, *Journal of Catalysis*, Vol.237, No.2, 2006, pp. 393-404.

[50] S. Wang, D. Song, L. Liao, M. Li, Z. Li, W. Zhou, Surface and Interface Engineering of BiOCl Nanomaterials and their Photocatalytic Applications, *Advances in Colloid and Interface Science*, Vol.324, 2024, 103088.

[51] Y. Zhang, X. Guo, W. Si, L. Jia, X. Qian, Ratiometric and Water-Soluble Fluorescent Zinc Sensor of Carboxamidoquinoline with an Alkoxyethylamino Chain as Receptor, *Organic Letters*, Vol.10, No.3, 2008, pp. 473-476.

[52] L. Wang, J. Sun, J. Shi, T. Huang, K. Liu, Z. Tong, H. Zhang, Reinforced Built-in Electric Field and Mediated Schottky Barrier Height via Carbon Quantum Dots Electronic Bridges on $BiOBr/Ti_3C_2$ for Efficient Photocatalytic Quinolone Antibiotics Degradation, *Chemical Engineering Journal*, Vol.500, 2024, 157168.

[53] Y. Zhang, Q. Pei, J. Liang, T. Feng, X. Zhou, H. Mao, W. Zhang, Y. Hisaeda, X.-M. Song, Mesoporous TiO2-Based Photoanode Sensitized by BiOI and Investigation of Its Photovoltaic Behavior, *Langmuir*, Vol.31, No.37, 2015, pp. 10279–10284.

[54] S. Li, C. Jiang, Y. Zhang, J. Tian, H. Yang, C. Wang, J. Yan, X. Li, K. Lv, Y. Liu, Synergistic Effect of N Doping and Oxygen Vacancies over TiO_2 Nanosheets with Enhanced Photocatalytic

Removal of Tetracycline, *Catalysis Today*, Vol.440, 2024, 114830.

[55] Z. Hu, X. Li, S. Zhang, Q. Li, J. Fan, X. Qu, K. Lv, Fe_1/TiO_2 Hollow Microspheres: Fe and Ti Dual Active Sites Boosting the Photocatalytic Oxidation of NO, *Small*, Vol.16, 2020, e2004583.

[56] H. Li, J. Shang, Z. Ai, L. Zhang, Efficient Visible Light Nitrogen Fixation with BiOBr Nanosheets of Oxygen Vacancies on the Exposed {001} Facets, *Journal of the American Chemical Society*, Vol.137, No.19, 2015, pp. 6393–6399.

[57] J. Yang, H. Luo, K. He, X. Dong, X. Zhu, X. Jia, L. Cai, X. Ni, J. Chen, Morphological Modulation of Copper-Doped BiOBr Nanomaterial with Improved Visible Light Photocatalytic Activity for Drug-Resistant Bacteria Elimination, *Separation and Purification Technology*, Vol.368, 2025, 132981.

[58] F. Yu, M. Jin, Y. Zhang, C. Lei, L. Zhou, H. Zhu, B. Yu, Visible-Light-Driven Zr-MOF/BiOBr Heterojunction for the Efficient Synchronous Removal of Hexavalent Chromium and Rhodamine B from Wastewater, *ACS Omega*, Vol.7, No.29, 2022, pp. 25066–25077.

APPENDIX

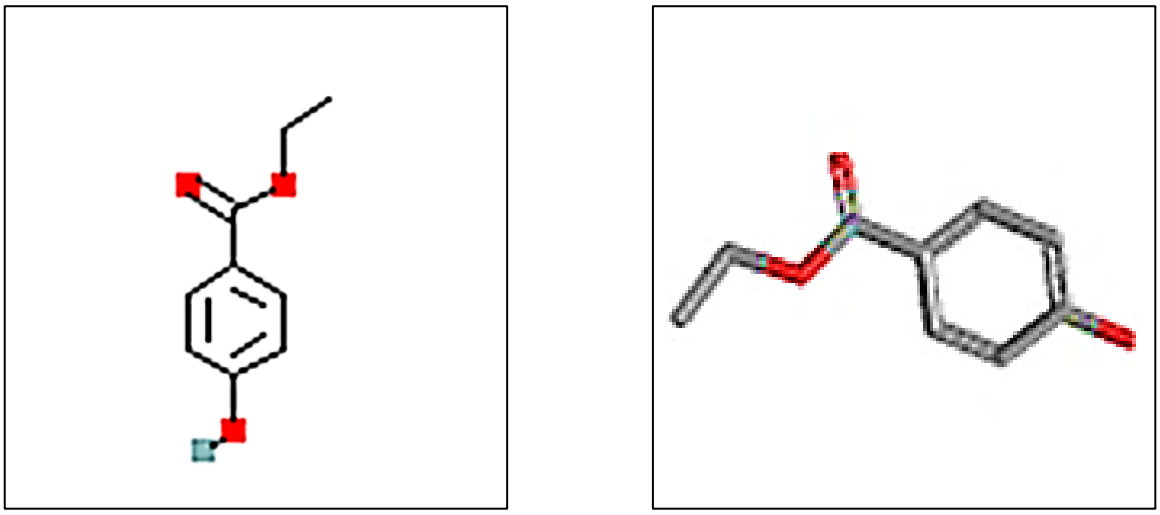

(a) **(b)**

Figure 1. The chemical structure of **(a)** Methyl-p-hydroxybenzoate and **(b)** Ethyl 4-hydroxybenzoate, respectively.

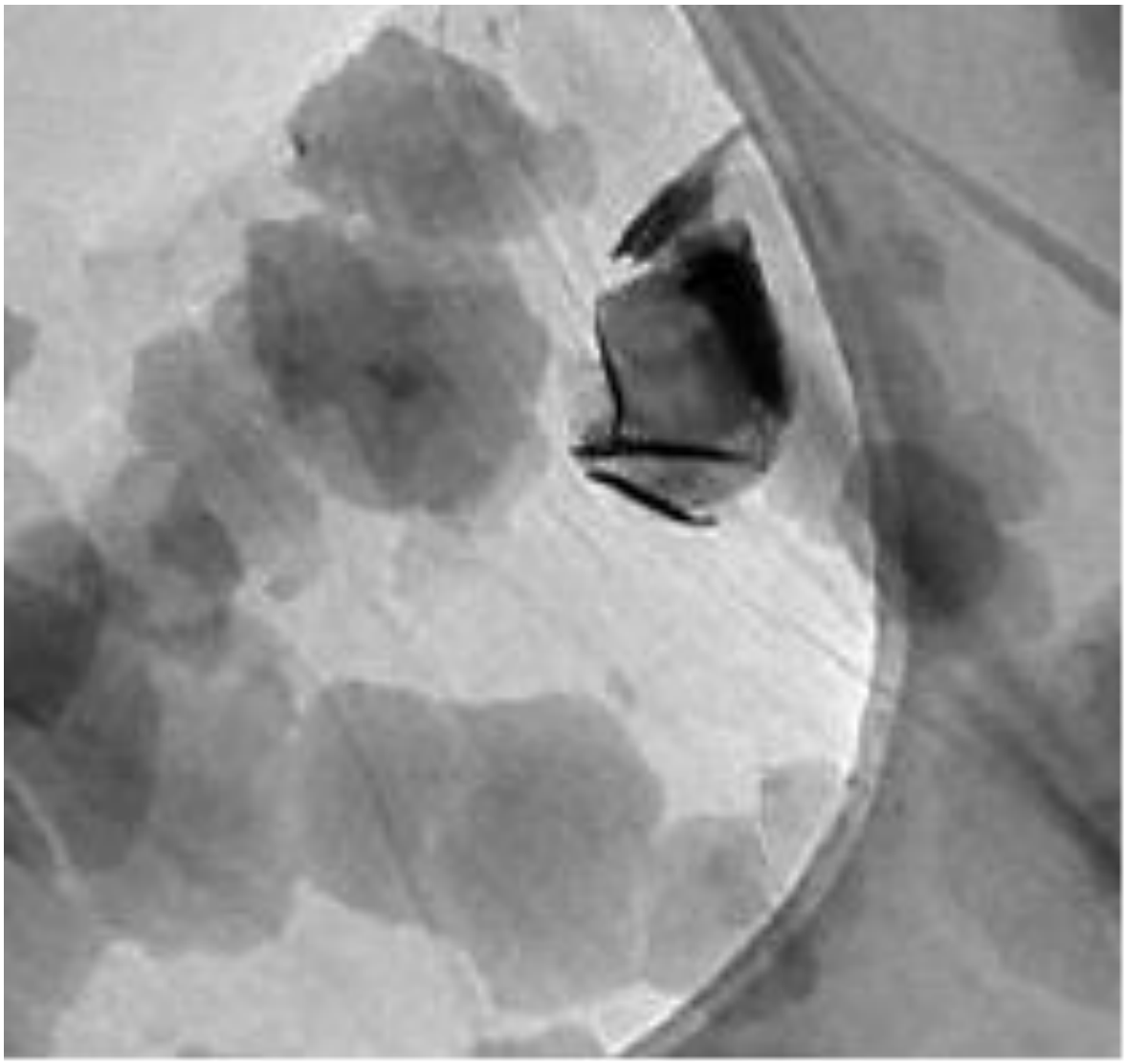

Figure 2. TEM spectra of N-doped BiOBr nanocomposites (TEM images size: 500 nm). (TEM image size: 100 μm).

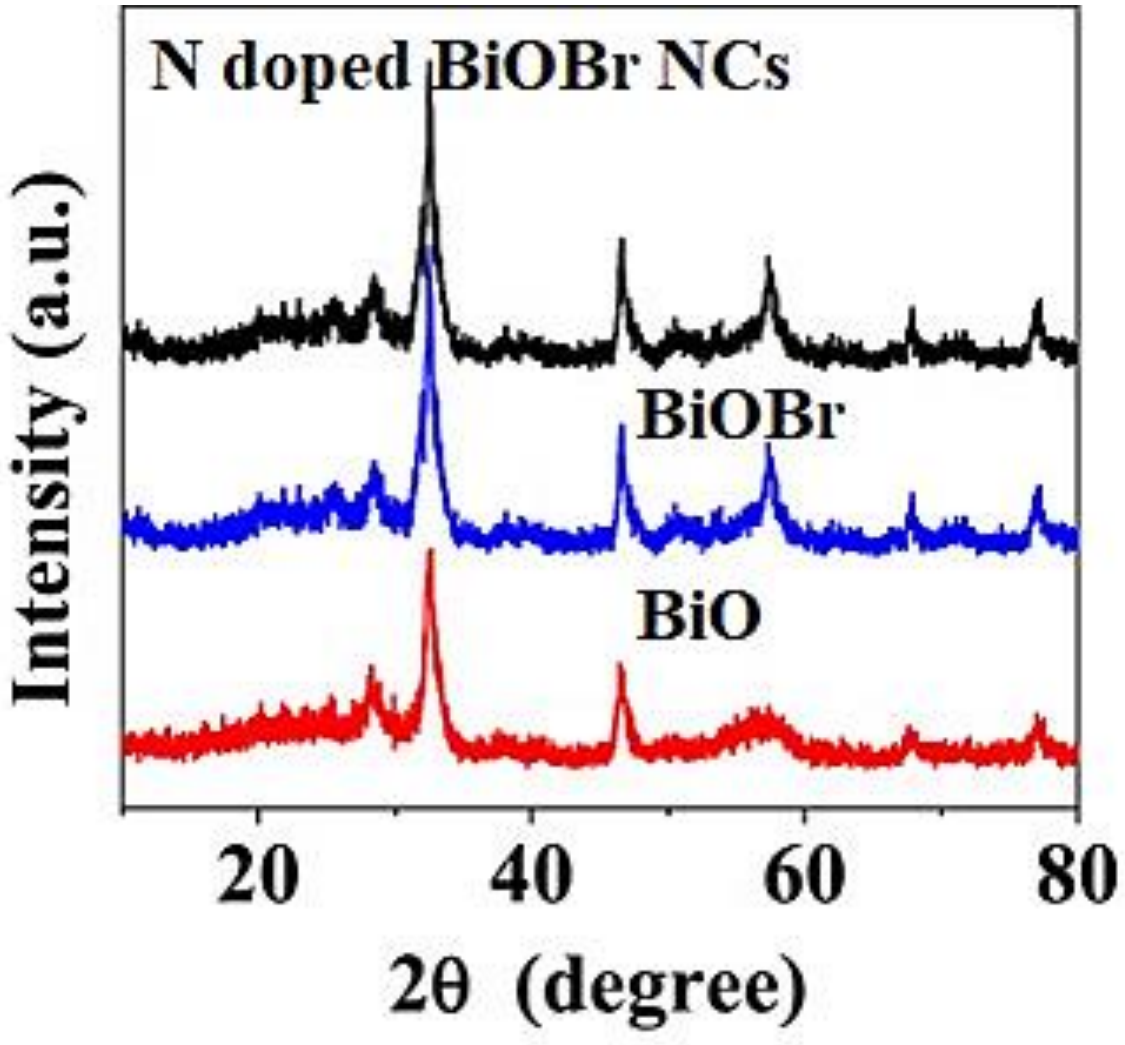

Figure 3. XRD patterns of BiO (red line), BiOBr (blue line) and N-doped BiOBr nanocomposites (black line), respectively.

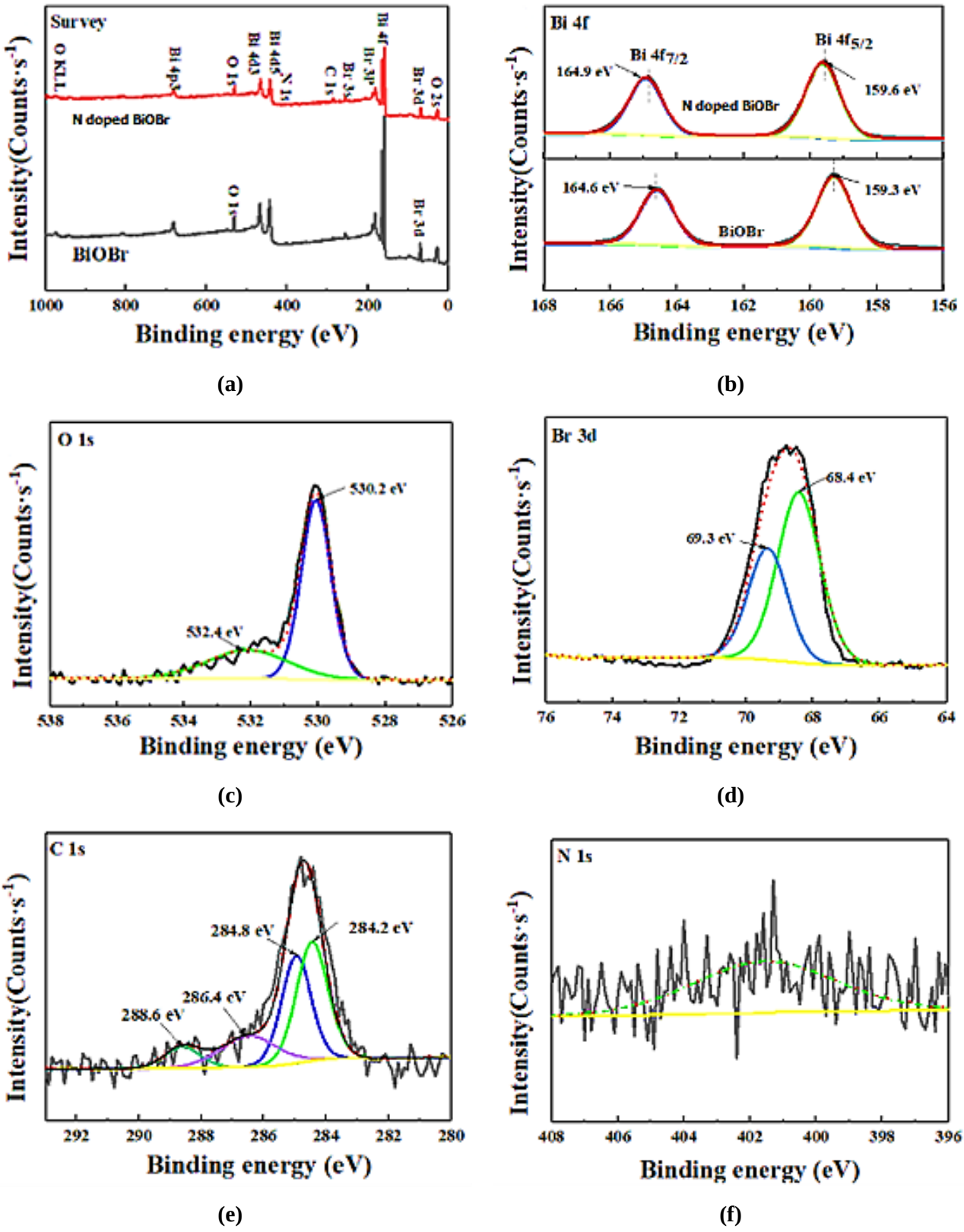

Figure 4. XPS results: **(a)** full scale; **(b)** Bi 4f of BiOBr and N-doped/BiOBr; **(c)** O 1s; **(d)** Br 3d, **(e)** C 1s, and **(f)** N 1s spectra of N-doped/BiOBr, respectively.

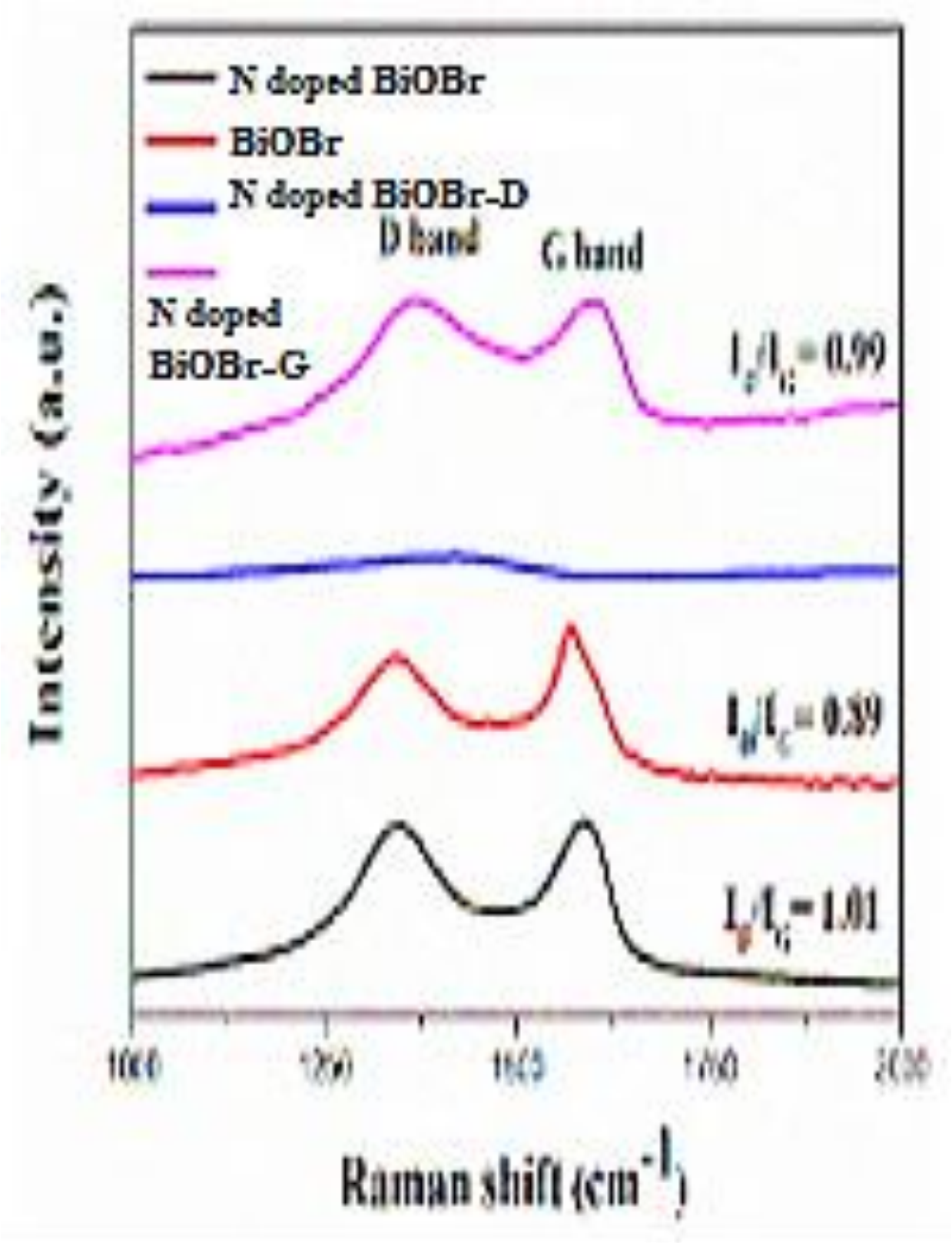

Figure 5. Raman absorption spectra of N doped BiOBr, BiOBr , N doped BiOBr-D, and N doped BiOBr-G, respectively.

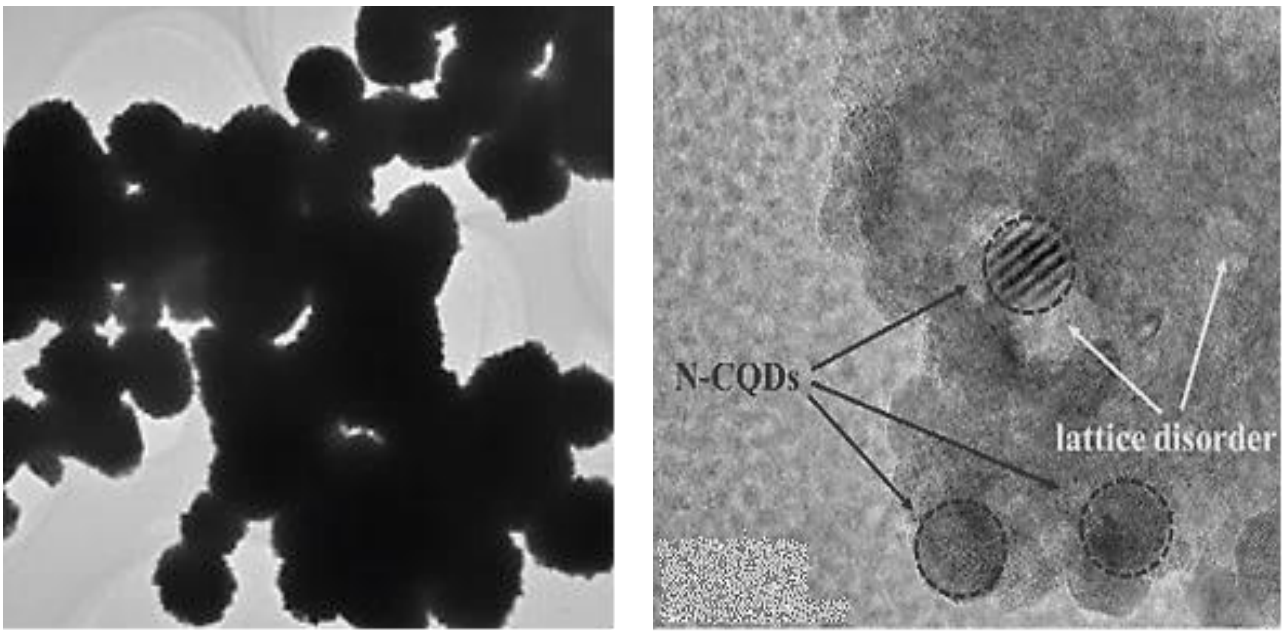

(a) **(b)**

Figure 6. The images of **(a)** HRTEM analysis of N-doped BiOBr nanocomposites and **(b)** SEM analysis of N doped BiOBr NCs, respectively. (HRTEM image size: 40 nm and SEM image size: 4 μm).

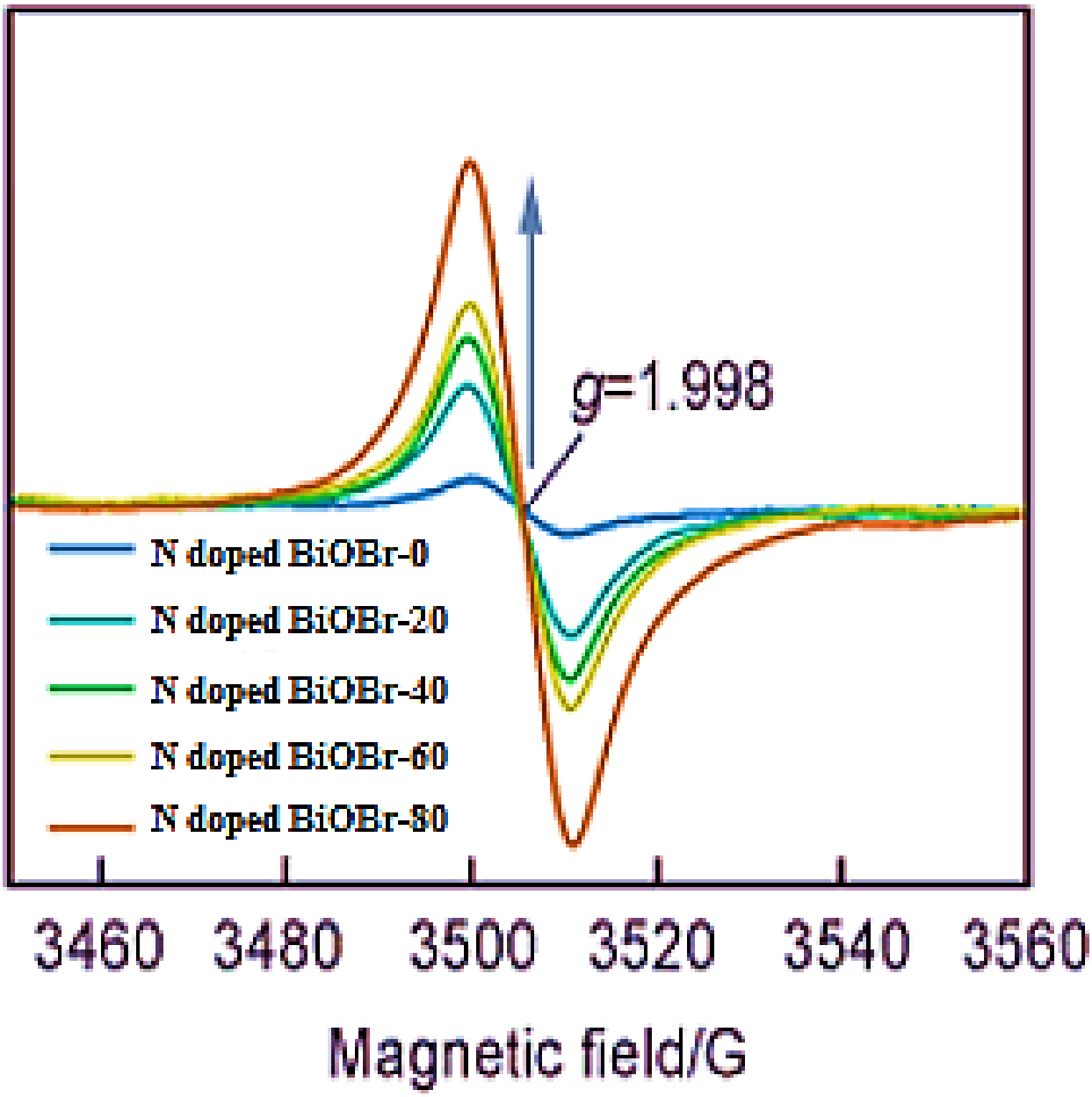

Figure 7. EPR spectra at increasing N-doped BiOBr NCs.

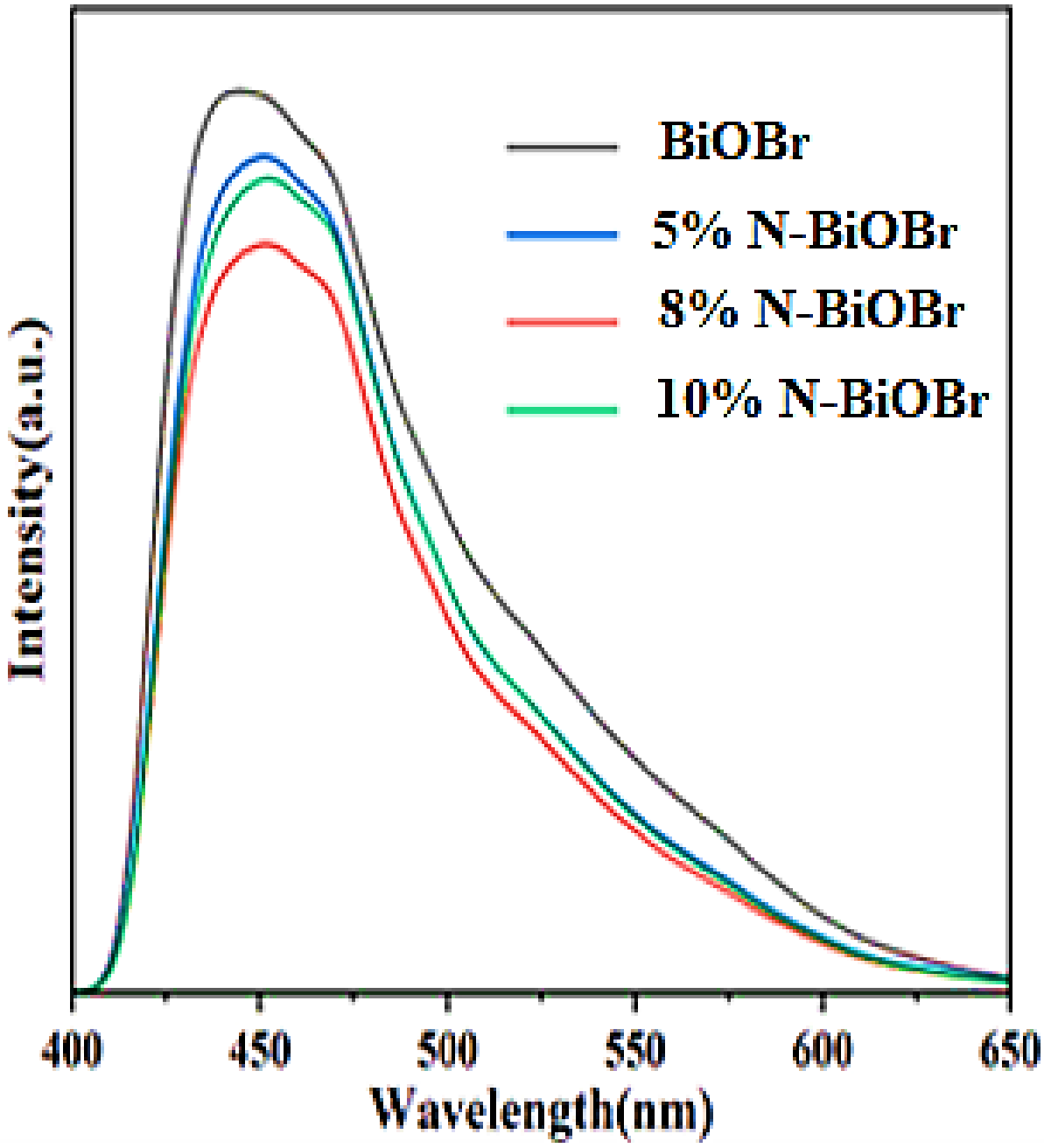

Figure 8. PL spectra of BiOBr and N-doped BiOBr NCs.

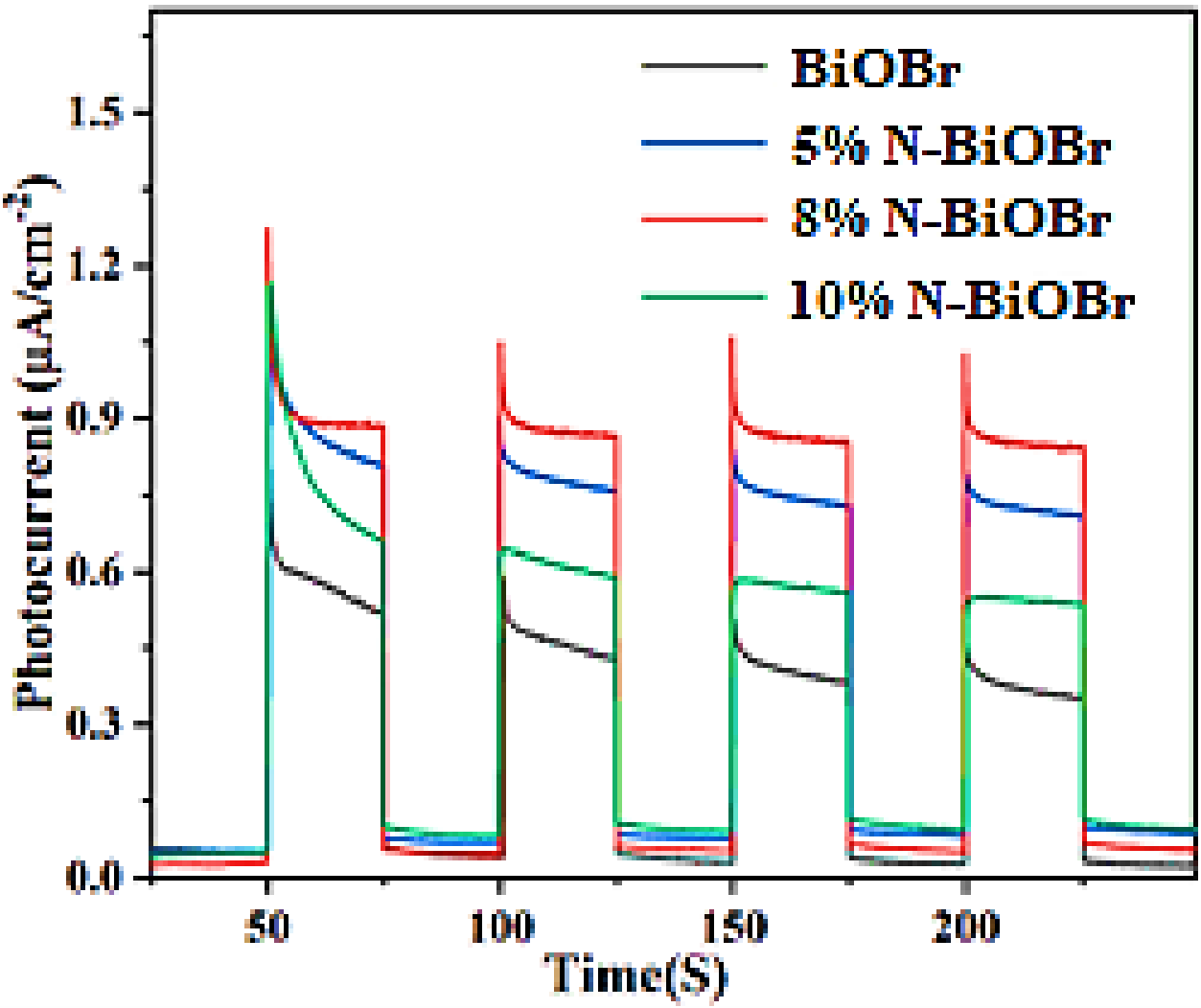

Figure 9. Photocurrent response spectra of BiOBr and N doped BiOBr samples.

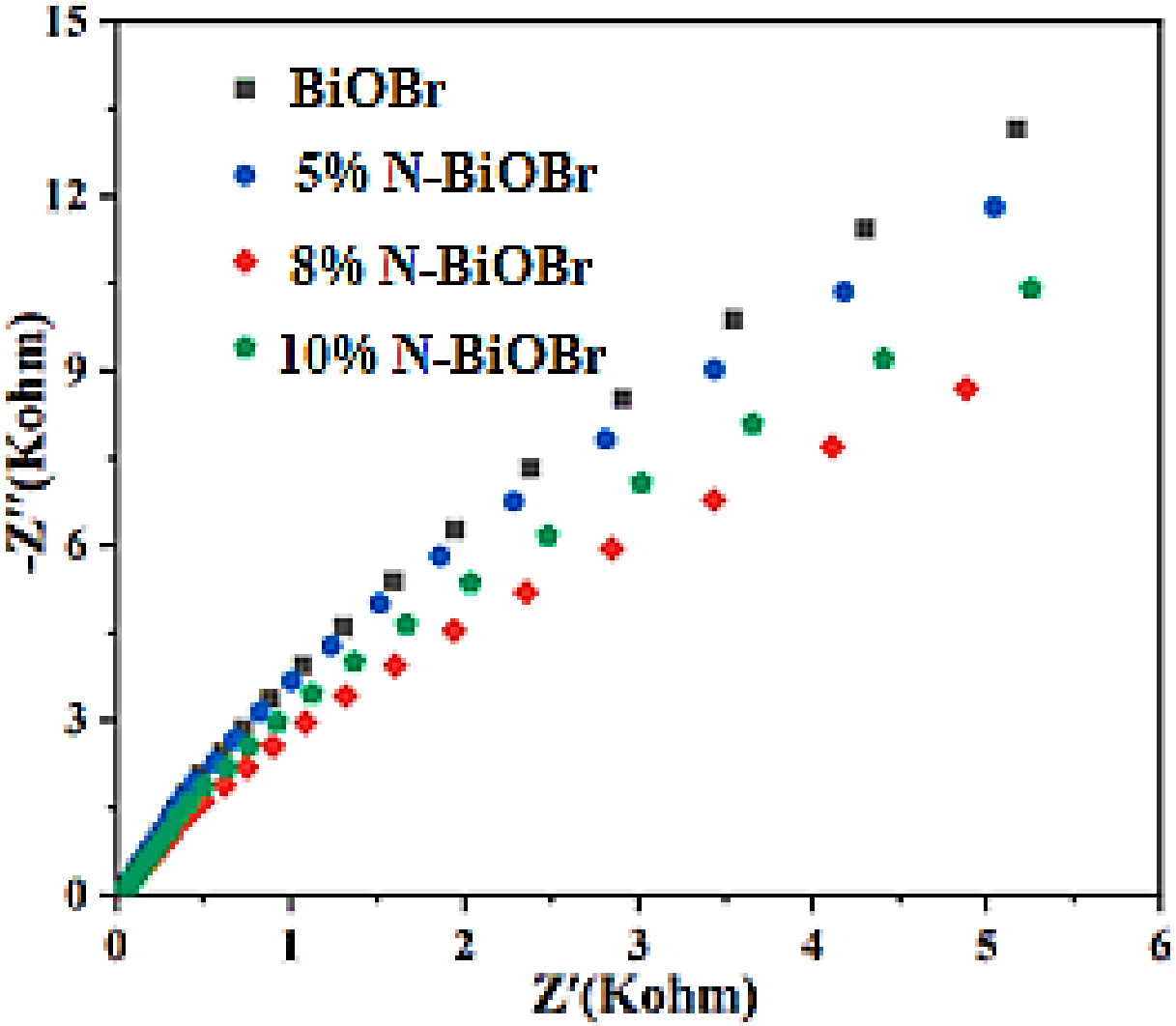

Figure 10. EIS spectra of BiOBr and N doped BiOBr NCs.

Table 1. Photodegradatıon of 45 mg/l of Methyl p-hydroxybenzoate and Ethyl 4-hydroxybenzoate with and without N doped BiOBr nanocatalysts (the N doped BiOBr nanocatalysts concentratıons were 2 mg/l and 3 mg/l wıth a N to BiOBr ratio of 8% after 25 min photodegradation time, at pH=7.0 and at 25^{o}C, respectively).

	N doped BiOBr Concentratıons and N to BiOBr Ratio			
	Without N doped BiOBr	Without N doped BiOBr	With 2 mg/l 8% vol. N doped BiOBr	With 3 mg/l of 8% vol. N doped BiOBr
Removal Efficiency (%)				
Methyl p-hydroxybenzoate	28% with Photolysis	32% with photolysis	97% with photodegradation	99% with photodegradation
Ethyl 4-hydroxybenzoate	28% with Photolysis	32% with Photolysis	97% with photodegradation	99% with photodegradation

Table 2. The effect of different N-doped BiOBr nanocomposites concentrations on the removal of 250 mg/l Methyl p-hydroxybenzoate, and Ethyl 4-hydroxybenzoate after 25 min photodegradation time, at pH=7.0 and 25^{o}C, respectively.

N-doped BiOBr Nanocomposites Concentration (mg/l)	**Photodegradation Removal Efficiencies (%)**	
	Methyl p-hydroxybenzoate (%)	**Ethyl 4-hydroxybenzoate (%)**
2	46	44
3	82	80
4	99	98
6	98	96

Table 3. The effect of increasing EDCs concentrations on the removals of Methyl p-hydroxybenzoate, and Ethyl 4-hydroxybenzoate yields after 25 min photodegradation time, at pH=7.0 and at 25ºC, respectively.

EDCs Concentration (mg/l)	**Removal Efficiencies (%)**	
	Methyl p-hydroxybenzoate (%)	**Ethyl 4-hydroxybenzoate (%)**
45	99	98
79	99	98
126	99	98
290	99	98
400	96	87

Table 4. The effect of increasing power on the removals of Methyl p-hydroxybenzoate, and Ethyl 4-hydroxybenzoate yields after 25 min photodegradation time, at pH=7.0 and at 25^{o}C, respectively.

Sun light power (W/m^2)	**Removal Efficiencies (%)**	
	Methyl p-hydroxybenzoate Yields (%)	**Ethyl 4-hydroxybenzoate Yields (%)**
2	30	28
4	52	51
8	99	98
10	98	96

Table 5. The effect of increasing temperatures on the removals of Methyl p-hydroxybenzoate, and Ethyl 4-hydroxybenzoate yields after 25 min photodegradation time, at pH=7.0 and at 25°C, respectively.

Temperature T(°C)	**Removal Efficiencies (%)**	
	Methyl p-hydroxybenzoate Yields (%)	**Ethyl 4-hydroxybenzoate Yields (%)**
20	78	76
25	99	96
30	84	81

Table 6. The effect of increasing pH values on the removals of Methyl p-hydroxybenzoate, and Ethyl 4-hydroxybenzoate yields after 25 min photodegradation time, at pH=7.0 and at 25^{o}C, respectively.

pH	Removal Efficiencies (%)	
	Methyl p-hydroxybenzoate Yields (%)	**Ethyl 4-hydroxybenzoate Yields (%)**
4.0	82	80
7.0	99	98
10.0	78	75
11.0	75	73

Table 7. Effect of increasing EDCs concentrations on *Daphnia magna* acute toxicity after photodegradation process, at 25ºC and at 35ºC.

No	Parameters	***Daphnia magna* Acute Toxicity Values, * EC (mg/l)**							
		25ºC							
		0. min		**10. min**		**20. min**		**25. min**	
		***EC_{50}**		***EC**		***EC**		***EC**	
1	Raw ww, control	850		EC_{45}=625		EC_{40}=370		EC_{29}=153	
		25ºC				**35ºC**			
		0. Min	**10. Min**	**20. min**	**25. min**	**0. min**	**10. min**	**20. min**	**25. min**
		***EC_{50}**	***EC**	***EC**	***EC**	***EC_{50}**	***EC**	***EC**	***EC**
2	Raw ww, control	850	EC_{39}= 468	EC_{34}= 228	EC_{23}= 111	850	EC_{34}= 373	EC_{29}= 210	EC_{18}= 71
3	EDCs=45 mg/l	850	EC_{33}= 449	EC_{23}= 144	EC_{18}= 259	850	EC_{33}= 129	EC_{18}= 424	EC_{13}= 339
	EDCs=79 mg/l	850	EC_{37}= 449	EC_{22}= 174	EC_{17}= 99	850	EC_{32}= 424	EC_{17}= 139	EC_{7}= 89
	EDCs=126 mg/l	850	EC_{33}= 349	EC_{18}= 239	EC_{13}= 89	850	EC_{28}= 149	EC_{13}= 59	EC_{8}= 17
	EDCs=290 mg/l	850	EC_{38}= 317	EC_{23}= 184	EC_{17}= 71	850	EC_{33}= 110	EC_{19}= 88	EC_{14}= 52
	EDCs=400 mg/l	850	EC_{43}= 299	EC_{28}= 169	EC_{23}= 51	850	EC_{38}= 249	EC_{23}= 109	EC_{18}= 10
* EC values were calculated based on COD_{dis} (mg/l).									

Table 8. L-H kinetics of pollutants

Temperature (oC)	**K_{LH} (m^3/mg)**	**k_s (mg/m^2.min)**	**R^2**
For Methyl p-hydroxybenzoate			
30	2.34	1.99	0.99
35	2.22	1.89	0.99
Ethyl 4-hydroxybenzoate			
30	2.29	1.86	0.99
35	2.19	1.80	0.99